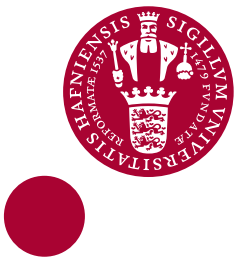

Structural Controls on Shallow Cenozoic Fluid Flow in the Otago Schist, New Zealand

Holbek, Simon C.; Frank, Madison; Scott, James M.; Smith, Steven A. F.; Le Roux, Petrus J.; Waight, Tod E.; Van Hale, Robert; Reid, Malcolm R.; Stirling, Claudine H.

Published in:
Geofluids

DOI:
10.1155/2020/9647197

Publication date:
2020

Document version
Publisher's PDF, also known as Version of record

Hindawi
Geofluids
Volume 2020, Article ID 9647197, 25 pages
https://doi.org/10.1155/2020/9647197

Research Article

Structural Controls on Shallow Cenozoic Fluid Flow in the Otago Schist, New Zealand

Simon C. Holbek,[1] **Madison Frank**,[1] **James M. Scott**,[1] **Steven A. F. Smith**,[1] **Petrus J. le Roux**,[2] **Tod E. Waight**,[3] **Robert Van Hale**,[4] **Malcolm R. Reid**,[4,5] **and Claudine H. Stirling**[4,5]

[1]*Department of Geology, University of Otago, Dunedin 9054, New Zealand*
[2]*Department of Geological Sciences, University of Cape Town, Rondebosch 7700, South Africa*
[3]*Department of Geosciences and Natural Resources Management (Geology Section), University of Copenhagen, Copenhagen K, Denmark*
[4]*Department of Chemistry, University of Otago, Dunedin 9054, New Zealand*
[5]*Centre for Trace Element Analysis, University of Otago, Dunedin 9054, New Zealand*

Correspondence should be addressed to Simon C. Holbek; simon.holbek@gmail.com

Received 14 October 2019; Revised 2 July 2020; Accepted 13 July 2020; Published 25 August 2020

Academic Editor: Antonio Benedicto

The Otago Schist in the South Island of New Zealand represents an exhumed Mesozoic accretionary prism. Two coastal areas (Akatore Creek and Bruce Rocks) south of Dunedin preserve structural and geochemical evidence for the development of postmetamorphic hydrothermal systems that involved widespread fluid-rock reaction at shallow crustal depths. The Jurassic to Triassic pumpellyite-actinolite (Akatore Creek) to upper greenschist facies (Bruce Rocks) metamorphic fabrics were crosscut by sets of regionally extensive Cretaceous exhumation joints. Many of the joints were subsequently reactivated to form networks of small-displacement (<metres) strike-slip faults containing cemented fault breccias and veins composed of hydrothermal calcite, siderite, and ankerite. Paleostress analysis performed on infrequent fault slickenlines indicates an overall strike-slip paleostress regime and a paleo-σ_1 orientation (azimuth 094°) similar to the contemporary σ_1 orientation in Otago and Canterbury (azimuth c. 110°-120°). High $\delta^{18}O$ values in vein calcite ($\delta^{18}O_{VPDB}$ = 21 to 28‰), together with the predominance of Type I calcite twins, suggest that vein formation occurred at low temperatures (<200°C) in the shallow crust and was associated with strongly channelized fluid flow along the joint and fault networks. Mass-balance calculations performed on samples from carbonate alteration zones show that significant mobilisation of elements occurred during fluid flow and fluid-rock reaction. Whole-rock and in situ carbonate $^{87}Sr/^{86}Sr$ data indicate varying degrees of interaction between the hydrothermal fluids and the host rock schists. Fluids were likely derived from the breakdown of metamorphic Ca-rich mineral phases with low ^{87}Rb in the host schists (e.g., epidote or calcite), as well as more radiogenic components such as mica. Overall, the field and geochemical data suggest that shallow fluid flow in the field areas was channelized along foliation surfaces, exhumation joints, and networks of brittle faults, and that these structures controlled the distribution of fluid-rock reactions and hydrothermal veins. The brittle fault networks and associated hydrothermal systems are interpreted to have formed after the onset of Early Miocene compression in the South Island and may represent the manifestation of fracturing and fluid flow associated with reverse reactivation of regional-scale faults such as the nearby Akatore Fault.

1. Introduction

Interactions between brittle faulting, fluid flow, alteration, and mineralization in the upper crust can strongly influence rock physical properties and strength [1–3], seismogenic potential and the distribution of earthquake sequences [4–6], and the evolution and geometry of mineralized zones. In the South Island of New Zealand, the timing and distribution

of fluid flow along basement-hosted brittle-ductile shear zones controlled the formation of ore deposits, especially orogenic gold deposits [7–11]. However, relatively few studies have been performed with the aim of establishing a structural and geochemical framework for fluid flow and mineralization events that occurred at relatively shallow crustal levels in regionally extensive basement schists.

The Otago Schist (Figure 1) contains well-studied examples of paleohydrothermal systems that developed within midcrustal faults and shear zones at various stages of regional metamorphism and exhumation [8–13]. However, there are also excellent examples of shallow paleohydrothermal systems that are relatively poorly understood. The purpose of this study is to determine the main structural and geochemical processes that influenced shallow fluid flow and mineralization within the Otago Schists. This will help to constrain the potential sources of fluids in shallow basement rocks, as well as the role of preexisting structures in controlling patterns of faulting and fluid flow. We characterise the structure and geochemistry of carbonate-bearing fault and vein networks and show that hydrothermal fluids were strongly channelized along brittle faults that developed in many cases by reactivation of preexisting exhumation joints. Whole-rock geochemistry, coupled with in situ mineral $^{87}Sr/^{86}Sr$, $\delta^{13}C$, and $\delta^{18}O$ analyses, enables the interpretation of fluid pathways and the main fluid-rock reactions that occurred during faulting.

2. Regional Geology and Active Tectonics

New Zealand is composed of two main geological provinces, the Western and Eastern Provinces, which are intruded by the Median Batholith [14, 15] (Figure 1(a)). Metasedimentary rocks in the Western Province define a series of tectonostratigraphic terranes that formed on the Cambrian to Ordovician Gondwana margin, which were subsequently intruded by plutonic rocks [16]. The Eastern Province, which contains the Otago Schists studied here, represents the forearc and accretionary prism to the Mesozoic Gondwana margin [16] (Figures 1(b) and 1(c)). Active tectonics in the South Island of New Zealand is dominated by the Alpine Fault system, which represents the present-day boundary between the Australian and Pacific Plates. Motion along the Alpine Fault is predominantly dextral strike-slip, but a significant component of dip-slip has caused formation of the Southern Alps mountain range and has resulted in te exhumation of the middle to upper crustal rocks at the surface (e.g., [17]).

Our study area on the coastline south of Dunedin City is in the Eastern Province Permian-Triassic Rakaia Terrane and Caples Terrane/Chrystalls Beach Complex (Figures 1(b) and 1(c)). These terranes were formed on the submarine convergent margin of Gondwana and are dominated by metaturbidites, although the Rakaia Terrane is slightly more SiO_2 rich than the Caples Terrane and is thought to have been derived from a more continental source [18]. The Chrystalls Beach Complex is a predominantly metasedimentary mélange that also contains rare metabasalts and metavolcanics and is interpreted as either an atypical part of the Caples Terrane or an intervening microterrane [19, 20]. The continental source for the Rakaia Terrane is suggested by whole-rock $^{87}Sr/^{86}Sr$ isotope data (at 135 Ma) that show it to be more radiogenic ($^{87}Sr/^{86}Sr_{(135\,Ma)} > 0.7065$) than the Caples Terrane ($^{87}Sr/^{86}Sr_{(135\,Ma)} < 0.7055$) or the Chrystalls Beach Complex (0.7052 and 0.7064) [21–25].

The Rakaia-Caples/Chrystalls Beach rocks experienced metamorphism and deformation within the Mesozoic accretionary prism, which led to formation of an expansive schist belt termed the Otago Schist (Figure 1(c)). The Otago Schist was metamorphosed at prehnite-pumpellyite to upper greenschist facies conditions between ~200 Ma and 135 Ma, with the metamorphic peak estimated to have been ~140-135 Ma [22, 26–28]. Crustal xenoliths in intraplate basalts indicate that the lower Otago crust was affected by granulite to ultra-high-temperature metamorphic conditions at ~92 Ma [29].

Progressive exhumation of the Mesozoic accretionary prism from the Early Cretaceous resulted in the formation of regionally extensive exhumation joints and associated fracture systems in the Otago Schist [28, 30, 31]. The orientation of these joints is mainly perpendicular to the metamorphic foliation and, in cases where a stretching lineation or metamorphic rodding is present, suborthogonal to the linear fabrics [31]. Joints are most abundant in greenschist facies rocks and less abundant at lower metamorphic grades (prehnite-pumpellyte facies) [31]. Following the development of the modern Alpine Fault plate boundary in the Early Miocene, much of the South Island of New Zealand experienced compressional inversion, which resulted in widespread reverse reactivation of normal faults that had initially formed in response to Late Cretaceous–Oligocene rifting and basin subsidence [32, 33]. One of the major reactivated faults is the Akatore Fault, which strikes NE-SW and dips steeply (c. 60-70°) to the SE in the study area (Figure 1(b)). The Akatore Fault is the easternmost onshore structure in the active Otago reverse fault province [34], which contains several active reverse faults striking NE-SW to NNE-SSW. The Akatore Fault hosted at least three M7.0 reverse-fault earthquakes between 13,317 B.C. and 1278 A.D [35].

Analysis of borehole breakouts and earthquake focal mechanisms indicates that the contemporary crustal stress field in the South Island is relatively homogenous and is characterized in most areas (including Otago) by a regional strike-slip stress regime (i.e., σ_2 is subvertical) and a maximum horizontal compressive stress axis (σ_1) between c. 110° and 120° [36–42]. This σ_1 orientation is broadly compatible with active reverse faulting along NE-NNE striking structures, although this would require σ_3 to be subvertical in a typical "Andersonian" faulting regime. Analysis of stress ratios throughout New Zealand shows that σ_2 is comparable in magnitude to σ_3 in the lower South Island, suggesting that switching between strike-slip and reverse-fault stress regimes may be possible [41]. A scenario in which $\sigma_1 > \sigma_{vertical} = \sigma_2 \sim \sigma_3$, with possible switching between stress regimes, was also suggested to explain the mixture of strike-slip and reverse fault ruptures observed during the 2010-2011 Canterbury earthquake sequence [40].

3. Analytical Methods

3.1. Paleostress Analysis of Brittle Faults. Win_TENSOR was used to determine paleostress orientations by analysing

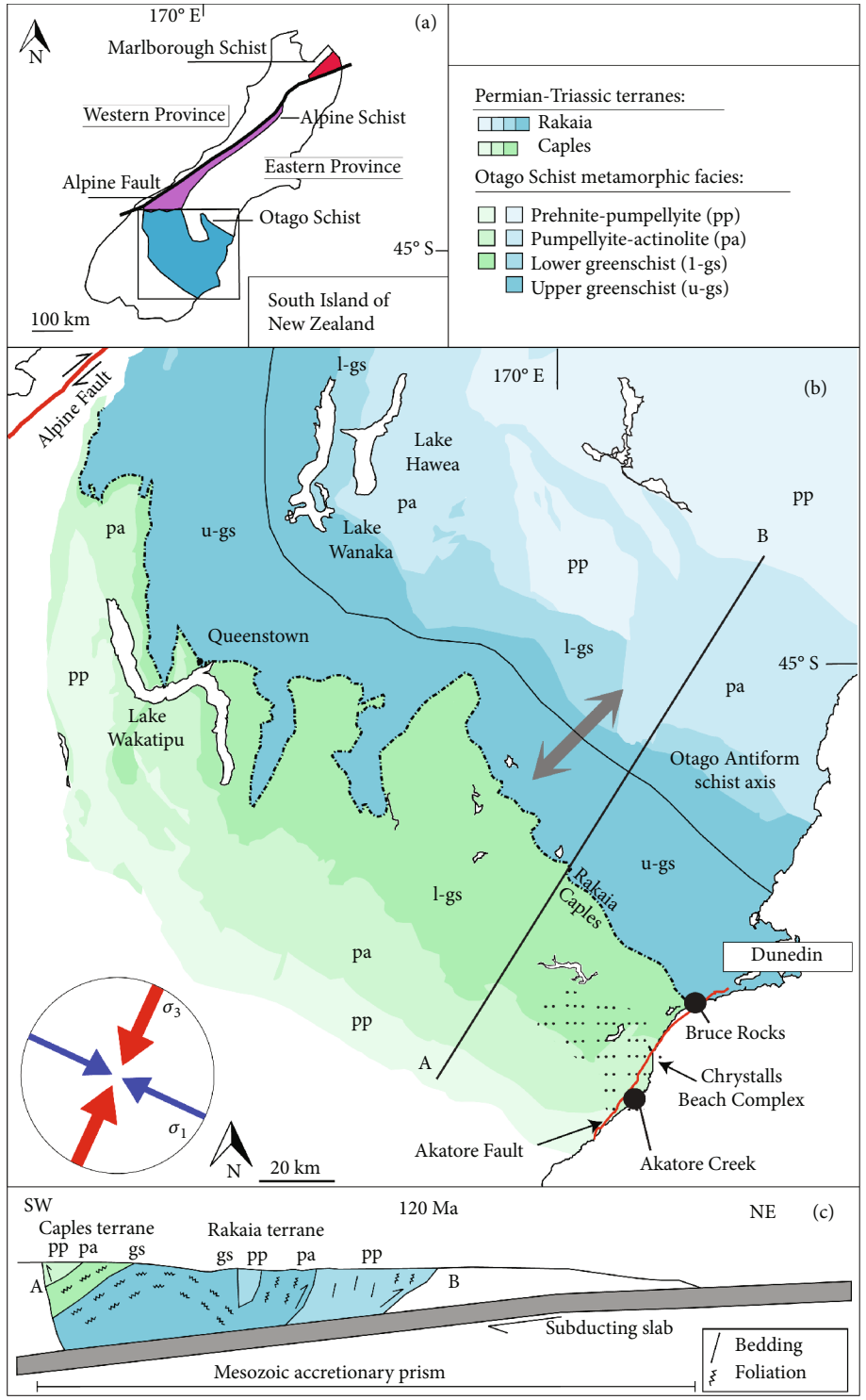

Figure 1: Geological setting of the field areas. (a) Simplified map of the South Island of New Zealand showing the Otago Schist and Alpine Schist. (b) Map showing the distribution of metamorphic facies in the Otago Schist, metamorphic terranes, the Chrystalls Beach Complex, and the Akatore Fault, together with the field locations at Akatore Creek and Bruce Rocks. Stereoplot in the bottom-left corner illustrates the modern-day strike-slip stress field in Otago and Canterbury as reconstructed from earthquake focal mechanisms and borehole breakout data (after [39] and [41]). (c) Simplified cross-section through the Otago Schist showing the regional scale antiformal structure. Schematic relationship to the Mesozoic accretionary prism is also shown [43].

slickenlines preserved on small-displacement fault surfaces [44]. Only ten strike-slip faults with slickenlines and unequivocal shear sense could be identified in the field due to poor preservation of kinematic indicators on schist-hosted fault surfaces. The small dataset limits interpretations of the paleostress conditions; however, a qualitative

comparison can be made between the reconstructed paleostress orientations and the contemporary stress field summarized in the previous section.

3.2. Geochemical Analysis of Carbonate Veins and Fault Rock Matrices. Major element compositions were determined in situ on single minerals using a JEOL JXA-8200 Superprobe at the University of Copenhagen, Denmark, and a Zeiss scanning electron microscope (SEM) at the University of Otago Micro and Nanoscale Imaging facility (OMNI). The Superprobe operated with an acceleration voltage of 15 kV, a beam current of 15 nA, and a spot size of 5 μm, whereas the SEM operated with an acceleration voltage of 15 kV and a beam current of 2.7 nA.

Whole-rock major and trace element compositions were determined by ALS Minerals in Brisbane, Australia, by inductively coupled plasma-atomic emission spectroscopy (ICP-AES) or by coupled plasma-atomic mass spectroscopy (ICP-MS). Loss on ignition (LOI) was measured by weighing one gram of sample powder, prior to and after experiencing 1000°C for one hour.

$^{143}Nd/^{144}Nd$ and $^{87}Sr/^{86}Sr$ whole-rock isotope data were measured at the University of Cape Town on a NuPlasma HR in the MC-ICP-MS Facility. Samples were dissolved in $HF:HNO_3$ solution for 48 hours at 140°C and subsequently dried down and converted to nitrate followed by standard chemistry to separated Nd and Sr [45, 46]. The reference standards were JNdi-1 for the Nd isotopes and NIST SRM987 for the Sr isotopes [47].

In situ trace element concentrations and Sr isotope data were measured using Laser Ablation Multiple Collector Inductively Coupled Plasma Mass Spectrometry (LA-MC-ICP-MS) in the Department of Chemistry, Centre for Trace Element Analysis, University of Otago. An Applied Spectra RESOlution 193 m laser ablation system with an M-50 laser ablation cell coupled to a Nu Plasma-HR MC-ICP-MS instrument collected data directly on thin sections. The instrument laser was operated with an on-sample fluence of 2.5 J/cm2 at a laser repetition rate at about 5 Hz with a stage propagation speed of 5-10 μm/s on a targeted area with data collected in time-resolved mode. The concentration of in situ trace elements was collected with a spot diameter of 50 μm, where the ablated material is ionised and measured by quadrupole ICP-MS. Reference materials were analysed repeatedly against NIST 610 glass and combined with measured Ca of carbonate mineral grains for corrections. In situ $^{87}Sr/^{86}Sr$ data were collected as line transects on thin sections at a propagation speed of 5-10 μm/s. A 2 Hz preablation run was programmed to clean the surface of the track before ablations, where He gas transferred the ablated material into the ICP-MS. Six collector chambers in the ICP-MS were set to collect material with atomic masses from 82 to 88, representing the masses of Sr, Rb, and Kr, and are used to correct the isotopic values measured, due to overlapping atomic masses between the isotopic element of Sr, Rb, and Kr. The Sr data were collected and reduced [48].

Target carbonate phases were microdrilled with a target weight up to 2000 μg ± 200 μg. $\delta^{13}C$ ($\delta^{13}C = 13C/^{12}C$) and $\delta^{18}O$ ($\delta^{18}O = 18O/^{16}O$) analyses were conducted on the Isotopic Ratio Mass Spectrometer (IRMS) with Thermo Delta Plus XP coupled to a trace GC ultra with a combi PAL autosampler at the Department of Chemistry, University of Otago. Samples were sealed and air was replaced by helium. Five drops of phosphoric acid were applied, followed by 100 μl aliquot of the evolved CO_2-He gas which was later extracted and injected into the IRMS. The standards NBS-18, IRU-Marble, and NBS-19 were used to calibrate the instrument and along with laboratory standards IRU-Marble and Atlantis3 (marine carbonate) to determine the precision and accuracy.

4. Results

4.1. Structural Geology of Akatore Creek and Bruce Rocks. Akatore Creek and Bruce Rocks are located on the southern limb of a regional-scale antiform in the dominantly quartzofeldspathic Otago Schist (Figure 1; [28, 49]). The main protolith lithologies to the Otago Schist are mudstone and sandstone, which are overprinted by a metamorphic foliation in both field areas. The combination of quartz, albite, chlorite, and muscovite, together with minor epidote, titanite, and calcite at Bruce Rocks indicates greenschist facies conditions, whereas the occurrence of pumpellyite at Akatore Creek indicates prehnite-pumpellyite facies metamorphic conditions [49]. Whole rock Ar-Ar and Rb-Sr data indicate that the metamorphic assemblages in both areas formed in the Late Jurassic to Early Cretaceous [22, 28, 49].

4.2. Metamorphic Foliation and Exhumation Joints. Foliation measurements in both field areas are tightly clustered. At Akatore Creek, the metamorphic foliation is shallowly east dipping, whereas at Bruce Rocks, the foliation dips moderately to the southwest (Figures 2(a) and 2(b)). The foliation in both areas is crosscut by pervasively developed sets of exhumation joints, interpreted to have formed during Early–Late Cretaceous exhumation due to release of residual elastic strain [31]. The joints commonly formed at large angles to the metamorphic foliation (Figures 2(c), 2(d), 3, 4(a), and 4(b)) and are relatively planar for distances of metres to tens of metres (Figure 3). The spacing between adjacent joints varies from a few centimetres to a few metres (Figures 3, 4(a), and 4(b)). At Akatore Creek, there are three main sets of exhumation joints that are all steeply dipping (Figures 2(c), 3, and 4(a)): (set 1) SE-NW striking, (set 2) E-W striking, and (set 3) N-S striking. At Bruce Rocks, the joints form one main set that strikes E-W and is moderately to steeply N-dipping (Figures 2(d) and 4(b)). Joints frequently occur with stepped geometries, where the tips of adjacent joints overlap by a few centimetres to tens of centimetres.

4.3. Brittle Faults Containing Carbonate Veins and Carbonate-Cemented Breccias. Many of the exhumation joints were reactivated as small displacement strike-slip faults, which are present as networks of linked faults visible across the coastal platforms (Figure 3). Thus, many of the brittle faults inherited the orientations and relatively planar nature of the preexisting joints (Figures 2(e), 2(f), 3, and 4).

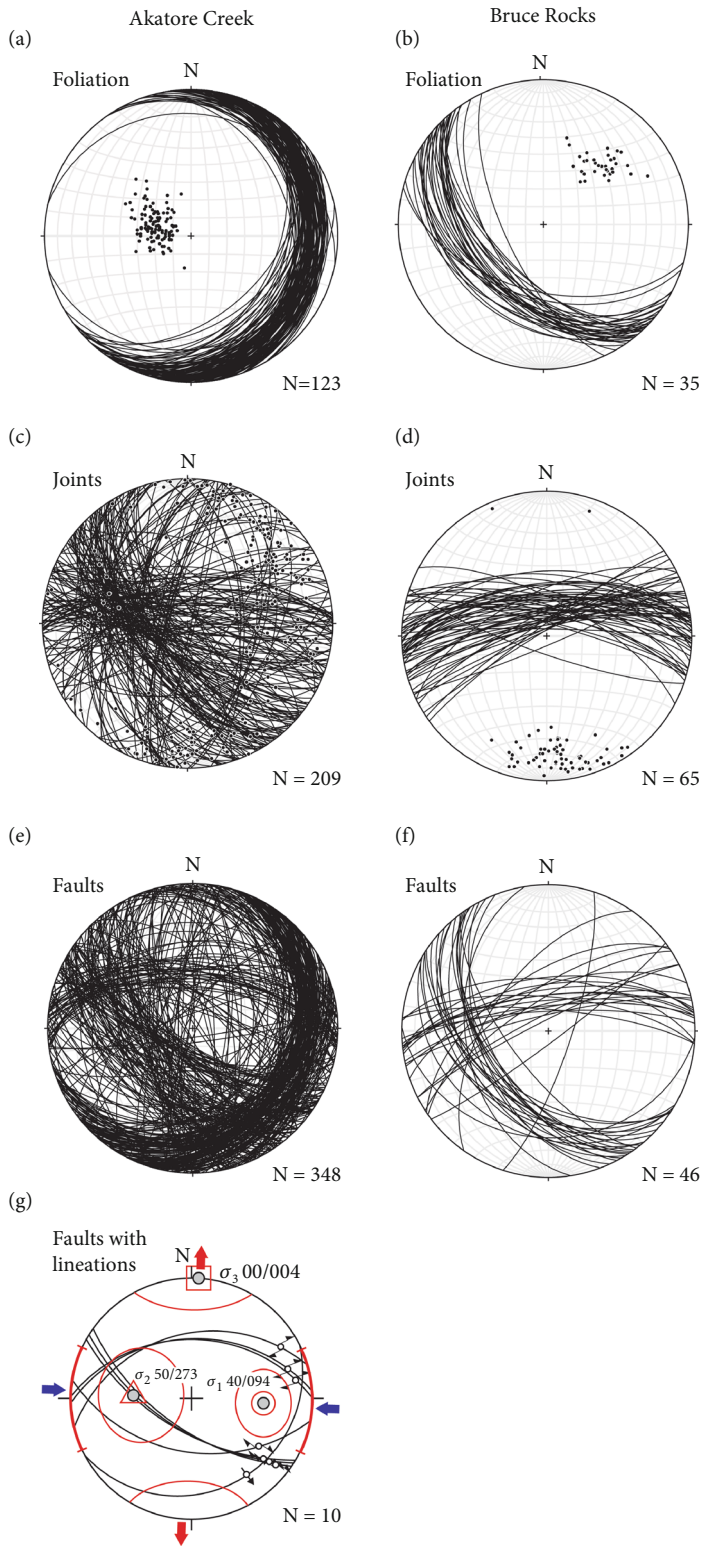

FIGURE 2: Structural data from Akatore Creek (left column) and Bruce Rocks (right column). All stereonets are equal-area, lower hemisphere. (a, b) Metamorphic foliation (Jurassic/Triassic). (c, d) exhumation joints (late Cretaceous). (e, f) Small-displacement brittle faults containing carbonate veins and carbonate-cemented fault breccias. (g) Paleostress analysis performed on ten small-displacement faults using WinTensor: three N-dipping dextral faults and seven S- to SW-dipping sinistral faults. The calculated orientations of the three principal stress axes are shown, and the associated uncertainties as the red ellipses.

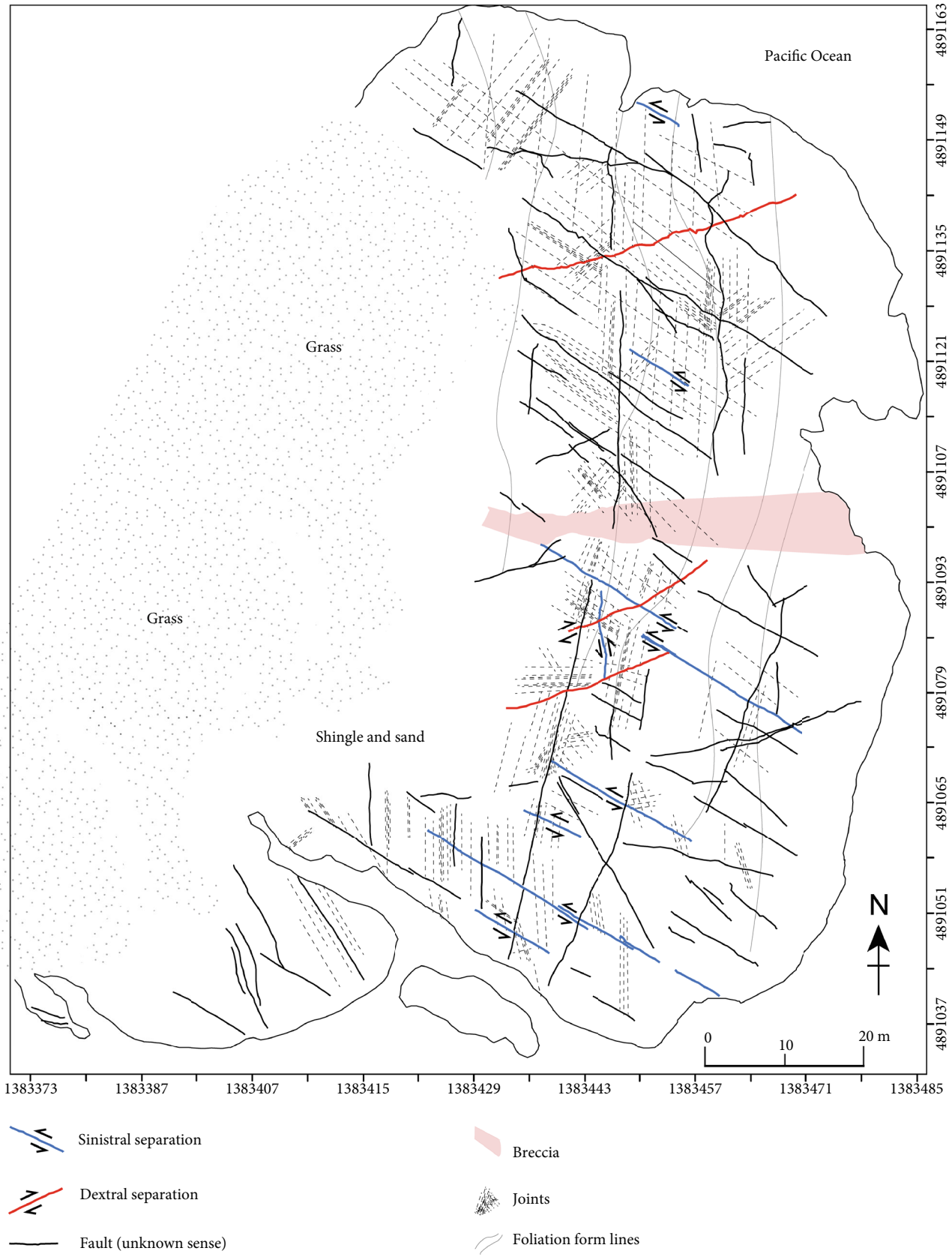

Figure 3: Detailed geological map of a coastal exposure approximately 2 km to the north of Akatore Creek. Grid references are NZTM. The map highlights the distribution and orientation of the metamorphic foliation, exhumation joints, and small-displacement strike-slip faults.

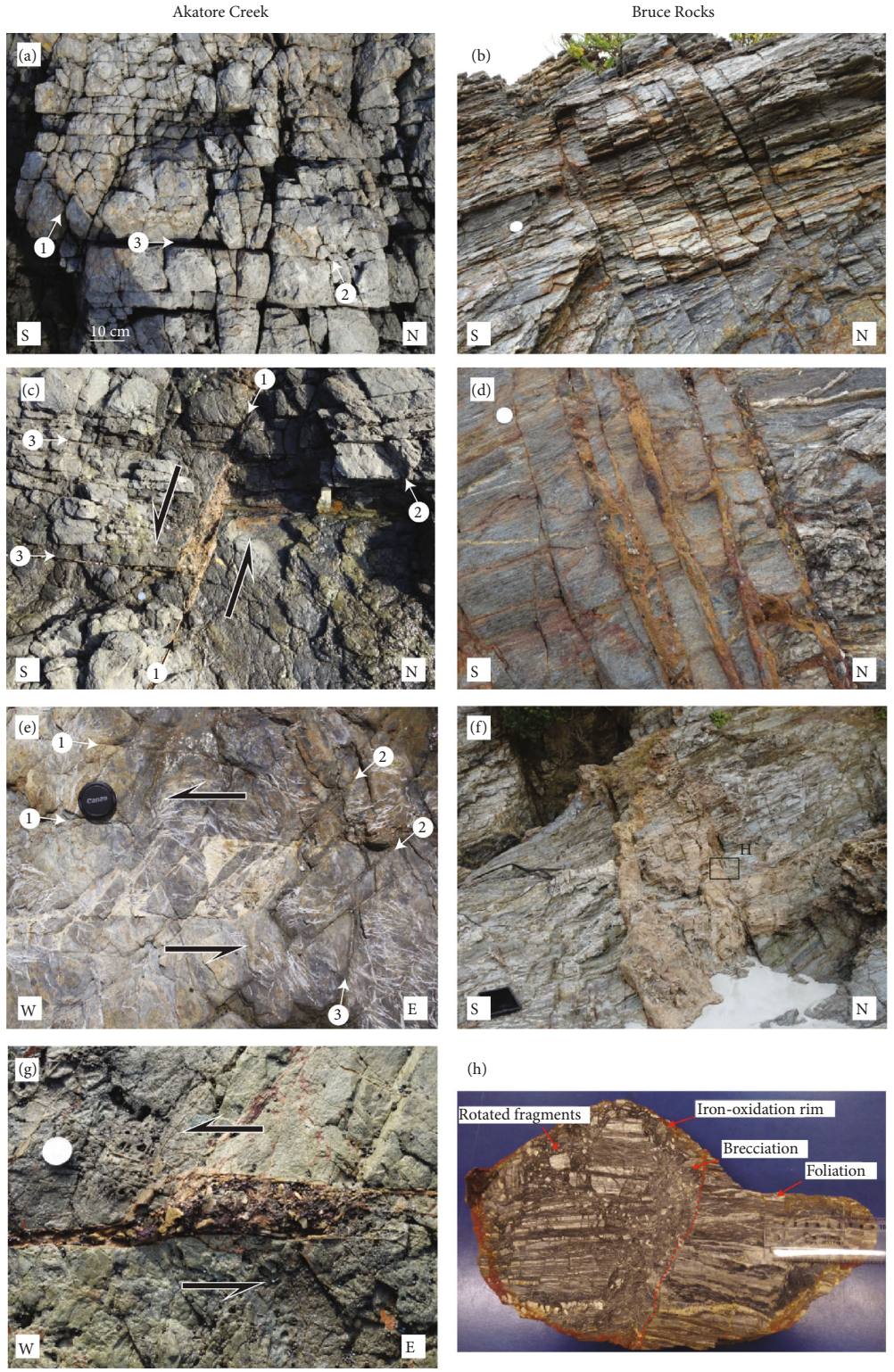

Figure 4: Photos from Akatore Creek (left column) and Bruce Rocks (right column). (a) Three main sets of exhumation joints are mutually intersecting at Akatore Creek. Spacing of joints varies between a few centimetres (in this photo) and a few metres (Figure 3). (b) One main set of steeply N-dipping joints at Bruce Rocks cuts across the prominent metamorphic foliation. (c) Reactivation of joint sets 1 and 3 has formed a carbonate-filled dilational jog. Joint set 2 is not reactivated in this case. (d) Reactivation of joints at Bruce rocks produce tabular layers of orange, carbonate-cemented fault breccias. (e) Formation of a rhomb-shaped carbonate-filled mosaic breccia at Akatore Creek, by reactivation of joint sets 1 and 2. (f) A relatively large fault at Bruce Rocks is surrounded by an orange, carbonate-bearing alteration zone. (g) Rhomb-shaped fault breccia at Akatore Creek containing fragments of calcite veins. (h) Polished hand specimen of fault breccia from Bruce Rocks, containing rotated angular fragments of Otago Schist.

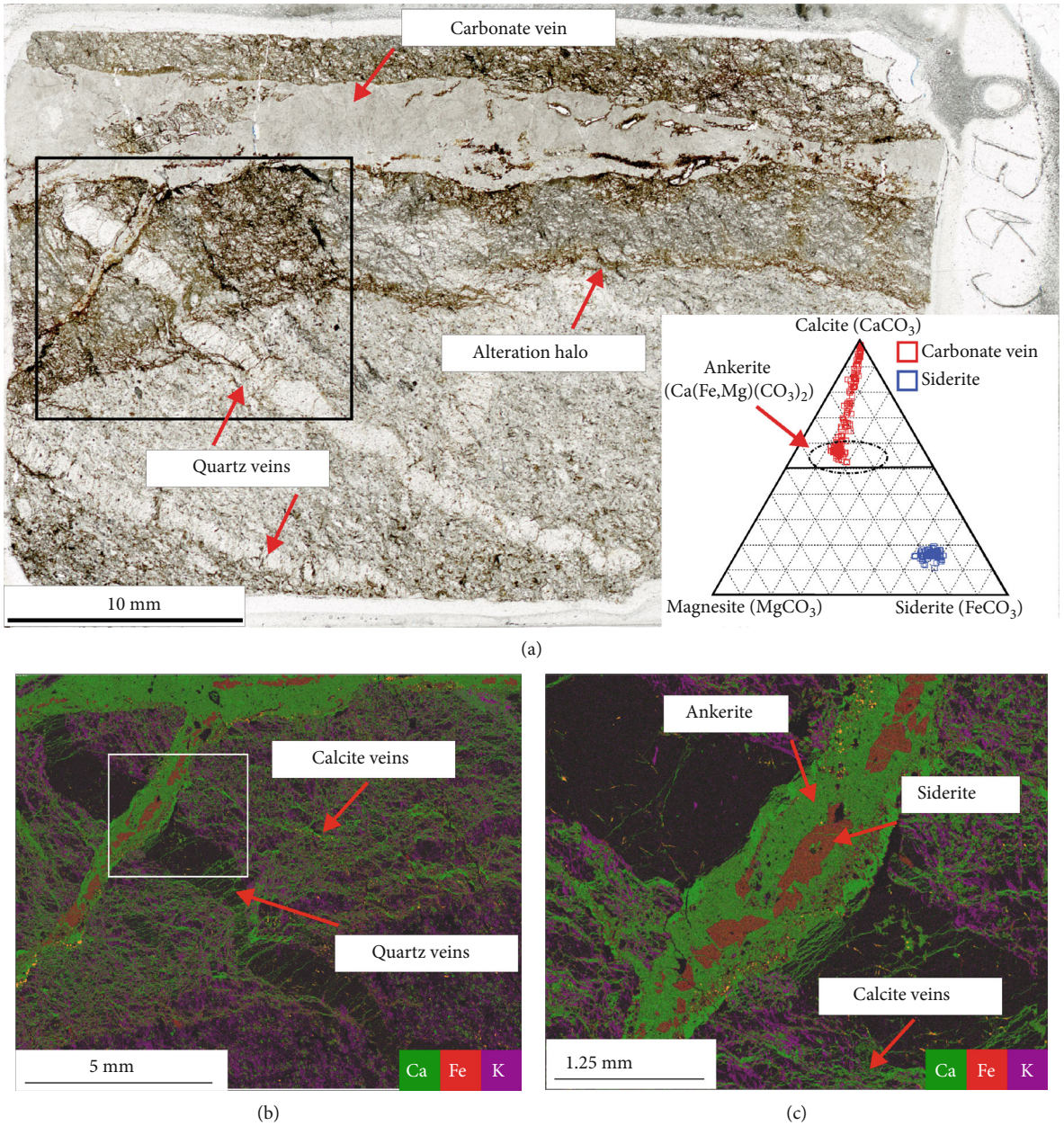

Figure 5: Geochemistry and mineralogy of hydrothermal carbonate veins. (a) Scan of a thin section of a hydrothermal carbonate vein from the altered greyschist showing a distinct alteration zone with cross-cutting segmented quartz veins. Ternary diagram of magnesite-calcite-siderite, showing the compositions of the carbonate veins. The carbonate vein shows a compositional variation between calcite and ankerite. (b) Element map (Ca, Fe, and K) of the carbonate vein and alteration zone (location in (a)) showing a network of thin calcite veins defining the alteration zone. (c) Close-up element map of the white box in (b), showing a carbonate vein containing ankerite, siderite, and calcite.

At Akatore Creek, the two dominant sets of steeply dipping faults (SE-NW striking and E-W striking) have similar orientations to the main sets of exhumation joints (Figures 2(e), 3, 4(c), and 4(e)). Where the kinematics and shear sense of the steeply dipping faults could be determined ($n = 10$), they show that the faults form conjugate sets of strike-slip to slightly oblique-slip faults (Figures 2(g) and 3). Analysis of paleostress using infrequent slickenlines preserved on fault surfaces at Akatore Creek gives the following principal paleostress orientations: $\sigma_1 = 40°/094°$, $\sigma_2 = 50°/273°$, and $\sigma_3 = 00°/004°$ (Figure 2(g)). In addition to the steeply dipping strike-slip faults, Akatore Creek also contains a set of faults that formed parallel to the metamorphic foliation (Figure 2(e)), but displacement and shear sense could not be determined for this set of faults. At Bruce Rocks, one of the dominant fault sets (E-W striking and steeply N-dipping) is inherited from preexisting exhumation joints, whereas the other set formed parallel to the metamorphic foliation (Figures 2(f) and 4(d)).

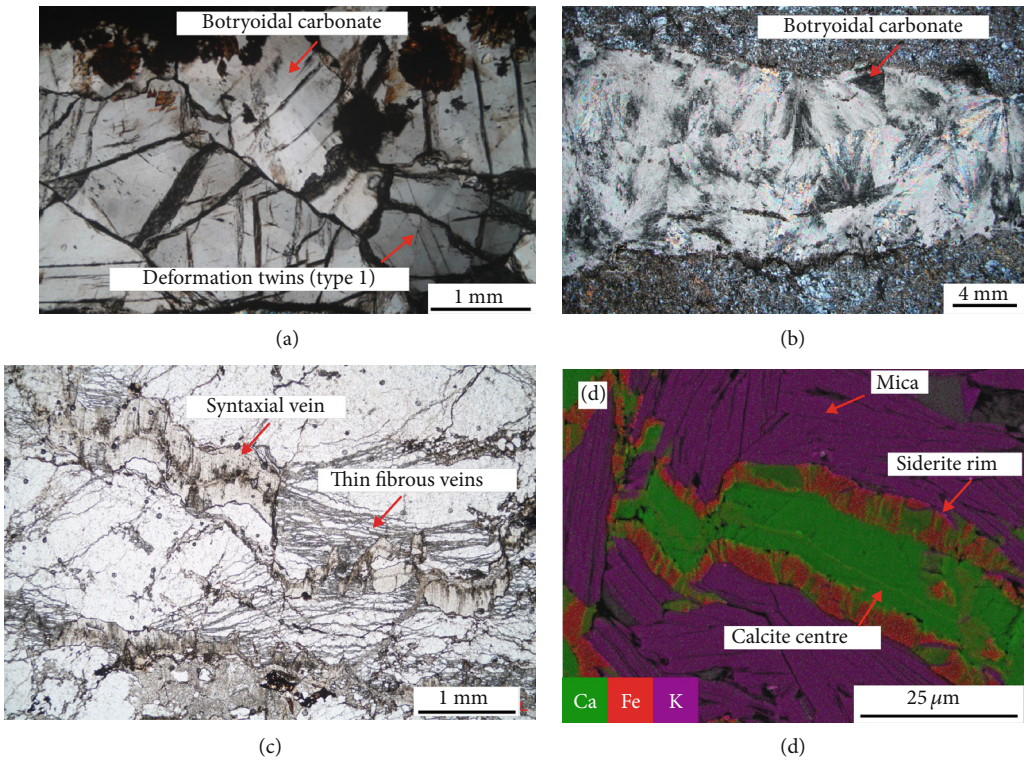

Figure 6: Microstructures of hydrothermal carbonate veins. (a) Botryoidal carbonate with rhombohedral cleavage and rare deformation twins (type 1) collected from Akatore Creek. (b) Botryoidal carbonate, from Bruce Rocks, with radiating grains fracturing parallel to the vein surface, without any sign of deformation twins. (c) Syntaxial veins and small fibrous veins in a quartzofeldspathic layer from the altered greyschist. (d) Ca, Fe, and K element map of a symmetric syntaxial vein in a mica-rich greyschist layer, showing a siderite rim and calcite centre.

In cases where joint tips overlapped, reactivation as small-displacement strike-slip faults resulted in the formation of rhombohedral-shaped dilational jogs filled by carbonate-cemented mosaic or crackle breccias (Figures 4(c), 4(e), and 4(g)). Small faults with displacements of less than a few centimetres typically contain thin (<cm) layers of cohesive carbonate-cemented breccia (Figure 4(d)) and/or thin (<mm) discontinuous carbonate veins. They can also be surrounded by orange-stained carbonate alteration zones up to a few centimetres wide. Faults that developed larger displacements contain layers of carbonate-cemented fault breccia up to a few tens of centimetres wide, which can be surrounded by orange-stained carbonate alteration zones up to a few metres wide (Figure 4(f)). The margins between fault breccias and the surrounding schist are typically sharp and planar (Figure 4(d)), which reflects the inherited planarity of the pre-existing joints. Well-developed fault breccias contain angular fragments of Otago Schist set in a matrix of hydrothermal carbonate and minor pyrite (Figures 4(g) and 4(h)).

4.4. Carbonate Geochemistry. Major element geochemistry indicates that several different compositions of hydrothermal carbonate are present within veins and the matrix of fault-related breccias (Figures 5 and 6): calcite (Ca wt.% = ~ 40), siderite (Fe wt.% = ~ 37), and ankerite, as well as intermediate compositions between calcite and ankerite (Ca wt.% = ~ 20–40, Fe + Mg wt.% = ~ 0–20). Ca, Fe, and K element maps reveal that carbonate alteration zones up to a few millimetres thick around small carbonate veins consist of fine-scale networks of very thin calcite veins with a fibrous texture (<200 μm; Figures 5(b) and 6(c)). Larger syntaxial veins (>0.5 mm: Figures 6(c) and 7(d)) are also present within the alteration zones; these often have siderite on the rim and calcite at the core (Figures 6(c) and 6(d)). Microscopic crosscutting relationships indicate that the syntaxial veins formed first, followed by the networks of fibrous calcite veins, which in turn were crosscut by the larger carbonate veins (Figure 5(b)). Nearly all of the carbonate phases from both study areas lack deformation twins, with the exception of infrequent Type I deformation twins, develops in botryoidal calcite from Akatore Creek (Figure 6(a); [50]).

LA-ICP-MS trace element spot analyses were collected on the hydrothermal carbonate-cemented breccias and the hydrothermally altered Otago Schist (Table 1). Trace element results show that the concentration of Sr is relatively low in siderite (BR2.E2A-2: <750 ppm; Table 1) and relatively high in fibrous calcite veins from the altered greyschists (AK34: >5000 ppm; Table 1). The Sr concentration is significantly higher in fibrous calcite veins from mica-rich greyschist layers (BR2.E2B: >2100 ppm; Table 1) compared to veins in quartzofeldspathic layers (BR2.E2C: <2100 ppm; Table 1) at Bruce Rocks. The concentration of rare earth elements (REE) in both study areas varies by up to three orders of magnitude ($\Sigma REE_{(N)}$ varies from >10 to <10000; Table 1). Rare

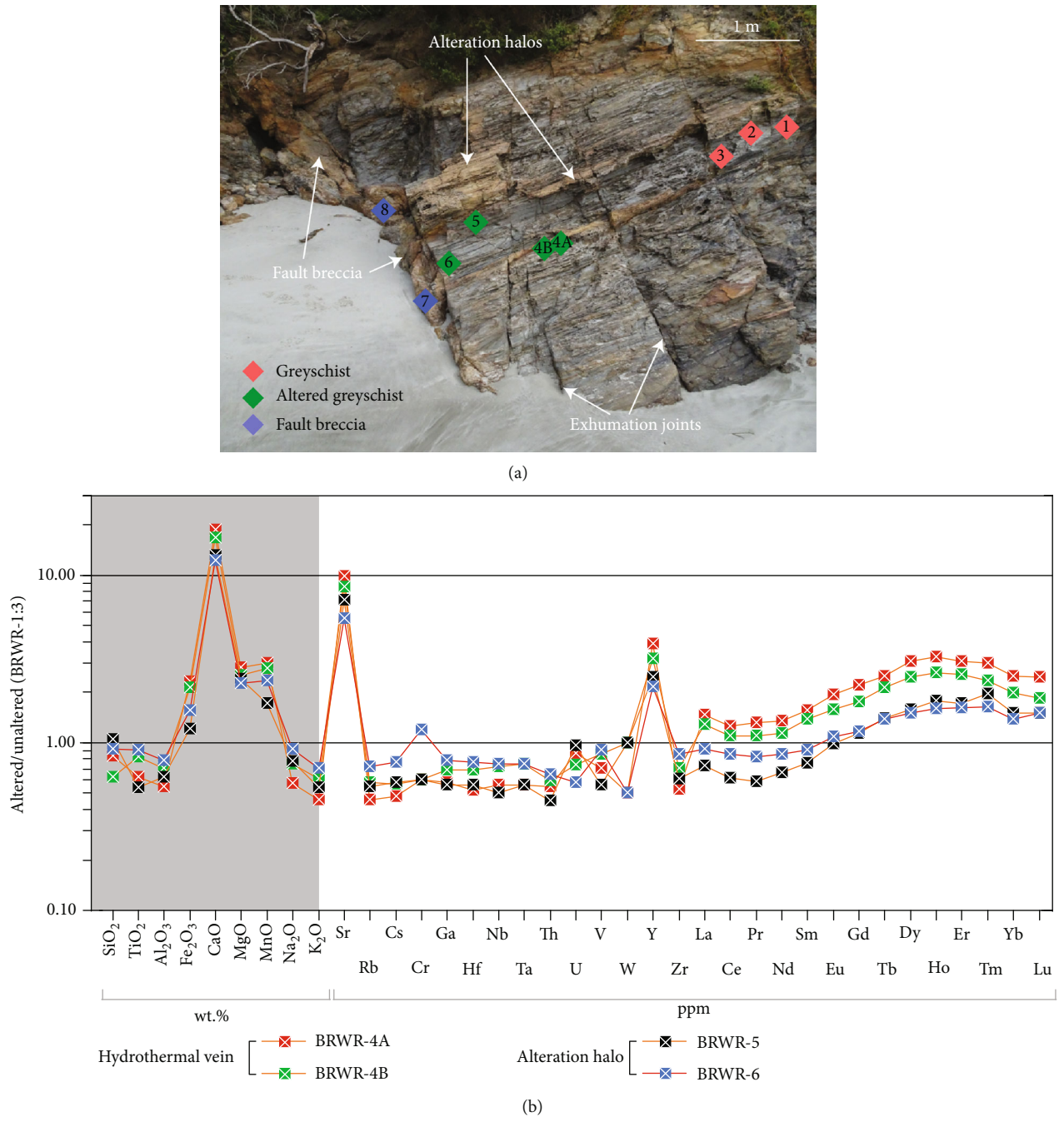

FIGURE 7: Whole-rock mass-balance calculations. (a) Outcrop at Bruce Rocks where samples were collected from unaltered grayschist (samples 1-3), altered greyschist from within carbonate alteration zones (samples 4-6), and fault breccia (samples 7-8). (b) Whole-rock geochemistry of the altered greyschist compared to the average of three unaltered greyschist samples (BRWR-1:3). Values higher than one are gained during alteration, and anything below one has been lost. The figure shows mobilization of Fe_2O_3, CaO, MgO, and MnO together with Sr, Y, and REE.

earth element patterns from carbonates in both study areas generally show light REE enrichment over heavy REEs ($La_{(N)}/La_{(N)} \geq 1$; Table 1). There is a general negative europium anomaly in both areas, with $Eu_{(N)}/Eu*_{(N)} \leq 1$ (Table 1; where $Eu_{(N)}/Eu*_{(N)} = Eu_{(N)}/(Sm_{(N)} \times Gd_{(N)})^{1/2}$). A few samples show heavy REE enrichment ($La(N)/Lu(N) \leq 1$; Table 1) and a slightly positive europium anomaly ($Eu(N)/Eu*(N) \geq 1$; Table 1), which could be due to contamination from other mineral phases such as plagioclase or zircon.

4.5. Elemental Composition of Alteration Zones. Samples for whole-rock major and trace element analyses were collected from an outcrop at Bruce Rocks composed of greyschist.

Table 1: In situ trace element compositions of hydrothermal carbonate from Akatore Creek and Bruce Rocks. Europium anomaly ($Eu_{(N)}/Eu^{*}_{(N)} = Eu_{(N)}/(Sm_{(N)} \times Gd_{(N)})^{1/2}$), LREE/HREE ($La_{(N)}/Lu_{(N)}$), and the sum of REEs ($\Sigma REE_{(N)}$) are calculated and normalised to CI–Condrite values [51].

(a)

Sample	AK17-1	AK17-2	AK17-3	AK23-1.	AK23-2.	AK23-3.	AK24-1.	AK24-2.	AK24-3.	AK33-1.	AK33-2.	AK33-3.	AK34-1.	AK34-2.	AK34-3.	AK40-1.	AK40-2.	AK40-3.	AK42-1.	AK42-2.	AK42-3.
P (ppm)	61.66	186	14.09	303	111	516	216	102	85.44	-	-	19.90	8.09	-		15.73	18.95	27.82	17.93	45.07	42.09
K	2129	1400	6.20	6816	2967	15.09	10111	10.05	12.82	8.23	9.66	15.44	10.73	14.74	15.45	13.67	17.61	9.41	7.77	37.71	85.51
Sc	7.70	3.41	4.31	12.83	22.94	35.29	31.42	22.67	20.70	1.01	2.62	7.22	-	0.12	1.06	0.42	0.36	0.37	5.11	3.86	25.56
Ti	1464	245	3.62	889	1792	5.49	1089	3.80	14.02	0.85	0.45	0.50	0.48	-	0.54	6.92	1.06	0.33	0.73	0.93	0.94
V	17.43	7.42	1.63	18.96	16.85	253	67.22	5.35	5.15	0.86	1.15	2.52	-	-	0.19	0.75	0.60	0.67	1.91	2.08	3.22
Cr	3.76	1.98	-	5.51	2.72	11.91	33.23	0.61	0.90	-	-	-	-	-	-	-		-	0.58	0.58	0.72
Mn	8076	9161	5836	8243	11481	958	1547	2337	2319	2673	2488	2653	363	54.41	541	2726	2938	2900	1831	2310	1664
Co	1.50	0.73	0.23	2.31	1.81	7.80	11.50	0.02	0.05	0.22	0.22	0.25	0.03	-	0.04	0.14	0.07	0.05	0.04	0.13	0.05
Ni	1.57	0.82	0.35	4.05	2.92	6.80	28.41	0.33	0.27	0.55	0.62	0.88	0.27	0.37	0.25	0.84	0.40	0.38	0.75	1.09	0.35
Cu	10.88	11.45	1.27	14.79	6.23	1.13	90.65	1.42	0.50	0.96	3.05	0.75	0.50	3.78	0.79	6.19	1.42	0.64	2.80	8.38	1.80
Zn	164	63.79	2.27	59.42	40.92	313	123	16.47	16.61	10.79	10.36	9.68	1.31	1.91	2.02	13.39	8.52	7.02	2.78	8.22	2.32
Ga	3.78	2.25	0.26	6.66	4.82	1.65	13.49	1.14	1.31	-	-	0.39	0.70	0.16	0.24	1.18	1.53	2.19	2.71	4.10	7.01
Rb	21.44	14.58	-	28.44	13.87	-	35.80	0.03	-	-	-	-	-	-	-	-	0.05	-	0.02	0.09	0.13
Sr	1387	1579	2629	1840	1668	1568	758	1359	1403	4458	4433	4396	5346	6888	9656	1066	717	588	1103	1211	1230
Y	46.82	23.04	12.25	104	185	318	76.11	108	99.52	6.84	19.91	53.56	127	116	17.50	65.73	80.67	122	176	554	490
Zr	28.20	13.07	5.12	11.20	24.95	825	75.17	108	98.82	0.76	1.82	1.83	0.09	0.03	0.36	2.76	1.41	1.22	0.08	0.49	0.32
Nb	5.68	0.76	-	1.89	4.18	-	2.14	-	0.04	-	-	-	-	-	-	0.02	-	-	-	-	-
Cs	17.68	9.04	-	6.40	7.85	-	11.61	-	-	-	0.01	-	-	-	0.00	-	-	-	-	-	0.02
Ba	171	157	246	482	358	65.13	135	34.80	17.50	296	283	284	1.35	0.59	6.79	20.55	13.65	12.68	1.37	2.94	4.21
La	71.34	39.84	8.24	66.76	91.96	27.06	64.54	50.39	51.48	0.20	1.66	11.69	25.99	11.94	7.08	56.08	77.37	105	121	184	279
Ce	122	63.52	17.86	141	178	78.85	113	82.82	87.10	0.53	3.49	21.96	44.27	14.12	15.63	79.36	115	155	199	294	495
Pr	16.26	7.97	2.81	16.53	22.55	11.92	13.69	10.48	10.91	0.09	0.51	2.79	5.63	1.51	2.16	9.62	13.64	18.67	24.13	37.13	60.11
Nd	69.25	33.38	13.06	65.26	97.66	65.47	55.31	45.13	45.80	0.38	2.37	12.61	26.28	6.34	9.20	41.89	56.81	82.26	96.45	162	248
Sm	14.50	6.36	2.62	14.96	24.19	23.08	11.90	9.93	9.83	0.12	0.57	3.33	8.76	2.49	2.02	8.48	11.15	16.14	20.26	43.34	59.03
Eu	2.69	1.14	0.50	4.73	6.91	6.90	3.31	2.23	2.30	0.06	0.18	0.92	2.21	0.91	0.37	1.92	2.81	3.71	5.14	11.63	13.88
Gd	13.99	6.47	2.52	16.60	27.95	37.13	12.70	12.11	10.96	0.21	0.90	5.02	17.46	9.16	1.96	9.89	12.78	19.36	24.99	66.80	72.24
Tb	1.66	0.78	0.27	2.55	4.41	6.25	1.87	1.85	1.71	0.03	0.17	0.81	3.00	1.82	0.25	1.22	1.46	2.35	3.64	11.07	12.17
Dy	8.63	4.00	1.55	16.63	29.15	44.72	12.11	13.41	12.60	0.38	1.46	6.50	21.56	14.77	1.75	7.20	8.83	13.82	22.75	74.80	80.06
Ho	1.43	0.64	0.34	3.15	5.65	9.56	2.39	2.98	2.82	0.09	0.37	1.50	4.41	3.61	0.36	1.39	1.73	2.77	4.32	14.62	15.75
Er	3.46	1.41	0.90	8.36	14.58	26.53	6.70	8.76	8.06	0.47	1.39	4.44	10.13	8.91	1.12	3.62	4.14	7.07	10.69	36.55	39.14
Tm	0.38	0.18	0.13	1.03	1.71	3.40	0.85	1.26	1.22	0.07	0.18	0.60	0.86	0.81	0.14	0.40	0.46	0.80	1.14	4.03	4.60
Yb	2.19	0.87	0.96	5.78	9.70	18.54	5.33	8.10	7.24	0.44	1.18	3.20	3.31	3.05	0.93	1.90	2.37	4.20	5.95	19.62	23.97
Lu	0.29	0.12	0.13	0.75	1.37	2.44	0.71	1.15	0.99	0.07	0.22	0.47	0.31	0.24	0.15	0.31	0.34	0.60	0.77	2.55	3.18
Hf	0.68	0.30	-	0.22	0.76	7.44	2.47	1.12	1.15	-	-	0.04	-	-	-	-	-	0.03	-	0.09	0.05
Ta	0.36	0.05	0.00	0.14	0.22	-	0.18	-	0.00	-	-	-	-	0.00	-	-	-	-	-	0.00	0.01
Pb	36.95	23.14	0.51	12.17	8.68	820	28.61	14.67	14.68	1.52	1.65	1.56	1.20	1.70	0.88	8.02	6.27	4.51	0.93	4.96	1.48
Th	6.85	2.69	2.66	40.96	39.54	7.43	6.28	1.50	3.96	-	0.05	0.93	0.07	0.22	0.57	1.23	0.28	0.13	2.08	0.24	9.29
U	4.61	1.25	3.67	3.18	1.87	8.48	2.26	3.82	3.69	0.16	0.34	1.97	0.11	0.04	0.16	7.45	5.08	4.24	4.16	2.21	6.06
$\Sigma REE_{(N)}$	1193	593	200	1430	2137	1970	1190	1067	1053	21.18	82.39	365	847	463	171	841	1138	1619	2075	4249	5730

Table 1: Continued.

Sample	AK17-1	AK17-2	AK17-3	AK23-1.	AK23-2.	AK23-3.	AK24-1.	AK24-2.	AK24-3.	AK33-1.	AK33-2.	AK33-3.	AK34-1.	AK34-2.	AK34-3.	AK40-1.	AK40-2.	AK40-3.	AK42-1.	AK42-2.	AK42-3.
$La_{(N)}/Lu_{(N)}$	25.92	36.51	6.96	9.49	7.22	1.19	9.72	4.71	5.58	0.29	0.81	2.68	9.06	5.28	4.94	19.22	24.58	18.69	16.73	7.74	9.40
$Eu_{(N)}/Eu*_{(N)}$	0.58	0.54	0.60	0.92	0.81	0.72	0.82	0.62	0.68	1.19	0.77	0.69	0.55	0.58	0.57	0.64	0.72	0.64	0.70	0.66	0.65

-: below detection limits (bdl).

(b)

Sample	BR2E.1	BR2E.2	BR2E.3	BR2E.4	BR2E.5	BR2E.6	BR2E.7	BR2E.8	BR2E.9	BR2E.10	BR2E.11	BR2E.12	BR2E2A.2-1	BR2E2A.2-2	BR2E2A.2-3	BR2E2B.1	BR2E2B.2	BR2E2B.3	BR2E2B.4	BR2E2B.5
P (ppm)	70.80	27.40	56.60	58.80	55.00	38.50	33.00	17.90	19.00	19.80	13.40	52.00	142	106	137	-	-	17.70	14.60	11.70
K	5.70	3.00	3.40	-	1.54	3.12	2.27	2.50	2.88	-	-	6.80	94.00	19.90	48.00	-	5.80	65.00	8.30	2.50
Sc	3.22	0.94	0.84	4.29	0.90	0.48	0.36	-	-	-	0.05	1.44	313	263	310	3.40	2.23	8.20	10.00	6.78
Ti	13.00	4.80	10.00	14.60	11.60	8.10	7.10	1.36	2.76	2.32	1.51	9.10	19.80	11.70	24.30	0.12	-	11.50	0.39	-
V	7.64	3.38	4.13	7.98	2.89	2.61	2.12	0.44	0.70	0.67	0.67	3.11	257	199	260	1.69	1.64	9.20	4.84	3.94
Cr	-	-	-		-	-	-	-	-	-	-	-	12.60	10.50	13.00	-	-	2.85	1.66	1.29
Mn	1630	1230	2007	1487	1567	1418	1205	437	504	484	500	1720	4530	3550	5040	641	639	928	720	620
Co	3.40	1.61	0.92	2.19	0.97	1.70	1.08	0.43	0.49	0.20	0.53	0.96	6.20	3.58	19.10	0.03	0.04	0.13	0.16	0.08
Ni	10.90	5.08	3.41	6.57	2.88	5.57	3.72	1.75	2.01	0.83	1.88	2.94	20.60	16.40	41.30	0.13	-	0.44	0.29	0.20
Cu	1.63	0.39	3.31	0.91	0.75	4.90	0.60	2.78	1.91	1.24	0.25	2.68	11.00	0.68	1.01	1.54	2.23	0.41	1.31	-
Zn	105	67.60	141	96.10	111	121	101	14.70	27.60	23.30	27.60	118	105	94.00	165	2.43	1.93	11.10	7.40	3.46
Ga	1.27	0.30	0.45	0.78	0.38	0.32	0.35	0.03	0.07	0.09	0.04	0.40	4.17	3.48	3.89	0.13	0.07	0.45	0.33	0.19
Rb	-	-	-	-	-	-	-	-	-	-	0.01	-	0.19	0.10	0.16	-	-	0.30	0.05	0.02
Sr	1664	984	1589	1568	1675	1289	1153	488	683	547	665	1655	703	614	640	3116	2971	2735	2396	2610
Y	53.60	17.60	8.85	42.80	16.24	15.54	17.40	1.44	5.75	5.31	1.81	15.57	876	722	830	18.89	15.61	37.20	30.79	24.29
Zr	2.19	4.68	5.10	3.29	3.17	3.33	3.03	1.56	1.46	1.65	1.31	3.80	1.26	1.14	2.22	2.65	1.55	7.53	4.03	1.51
Nb	0.00	0.00	-	-	0.00	-	-	-	-	-	-	-	0.01	0.01	0.01	-	-	0.01	-	-
Cs	-	-	-	-	-	-	-	-	0.00	-	-	-	-	-	-	-	-	0.03	0.01	-
Ba	57.20	36.40	91.30	61.90	77.40	70.60	54.00	14.20	19.30	16.00	20.60	77.20	125	99.90	122	65.40	61.80	117	94.40	59.50
La	73.00	14.50	12.77	40.30	14.30	11.38	8.97	0.54	1.90	1.40	0.60	12.39	221	188	210	8.55	6.15	29.90	24.70	14.49
Ce	141	20.50	25.40	83.30	27.20	18.04	13.64	0.66	2.81	1.78	0.84	23.10	422	369	429	14.65	11.09	47.80	42.10	26.60
Pr	17.10	2.44	2.86	10.18	3.22	2.22	1.75	0.11	0.37	0.24	0.11	2.83	51.80	45.30	50.50	1.85	1.40	5.44	4.72	3.37
Nd	72.40	11.20	12.14	45.70	14.70	10.27	7.71	0.47	2.18	1.36	0.61	12.38	248	212	244	8.89	6.82	22.30	20.70	14.51
Sm	14.70	2.29	2.54	9.50	3.14	2.18	1.87	0.09	0.48	0.34	0.14	2.54	70.00	61.20	70.00	1.95	1.46	4.80	4.11	3.28
Eu	4.34	0.69	0.78	2.82	0.94	0.66	0.59	0.04	0.12	0.14	0.04	0.72	26.70	21.80	27.20	0.68	0.50	1.35	1.25	1.01
Gd	13.40	2.58	2.04	9.20	2.82	2.19	2.29	0.14	0.69	0.48	0.22	2.43	94.20	82.90	95.00	2.26	1.92	5.17	4.36	3.68
Tb	1.91	0.35	0.31	1.28	0.47	0.33	0.32	0.02	0.08	0.08	0.02	0.39	18.80	16.20	19.40	0.35	0.37	0.83	0.67	0.57
Dy	10.49	2.47	1.58	8.20	2.46	1.96	2.17	0.14	0.48	0.53	0.17	2.65	135	111	131	2.37	2.09	5.33	4.40	3.53
Ho	1.83	0.48	0.28	1.55	0.49	0.43	0.45	0.03	0.12	0.10	0.03	0.45	31.40	26.40	30.70	0.58	0.46	1.07	0.91	0.73
Er	4.45	1.20	0.66	4.04	1.25	1.01	1.15	0.11	0.34	0.30	0.12	1.06	88.50	74.10	86.70	1.47	1.19	2.94	2.35	2.14
Tm	0.60	0.15	0.11	0.50	0.15	0.12	0.14	0.01	0.04	0.04	0.01	0.15	13.50	11.00	13.20	0.20	0.16	0.38	0.32	0.28
Yb	3.26	1.05	0.52	2.92	0.79	0.73	0.80	0.04	0.19	0.18	0.09	1.00	85.10	67.20	81.40	1.17	1.00	2.30	1.80	1.87
Lu	0.40	0.10	0.06	0.34	0.10	0.09	0.10	0.01	0.03	0.02	0.01	0.09	10.10	8.07	9.30	0.14	0.12	0.29	0.22	0.24
Hf	0.05	0.02	0.12	0.06	0.05	0.06	0.08	0.03	0.02	0.03	0.01	0.07	0.03	0.05	0.07	0.02	0.04	0.06	0.07	-
Ta	-	-	-	-	-	-	-	-	-	-	-	-	0.00	0.00	-	-	-	-	-	-

Table 1: Continued.

Sample	BR2E.1	BR2E.2	BR2E.3	BR2E.4	BR2E.5	BR2E.6	BR2E.7	BR2E.8	BR2E.9	BR2E.10	BR2E.11	BR2E.12	BR2E2A.2-1	BR2E2A.2-2	BR2E2A.2-3	BR2E2B.1	BR2E2B.2	BR2E2B.3	BR2E2B.4	BR2E2B.5
Pb	14.10	17.00	13.60	14.35	11.19	13.10	11.76	2.32	3.72	3.77	4.63	11.80	2.94	2.03	3.90	2.38	2.00	6.93	4.49	2.05
Th	6.15	0.83	4.29	23.70	3.03	0.18	0.03	-	-	-	0.01	6.32	18.00	13.40	18.50	1.37	0.56	3.79	4.91	1.66
U	1.44	1.79	0.18	0.80	0.20	10.00	3.63	21.10	6.71	7.84	5.74	0.56	4.52	3.57	4.18	0.01	0.01	0.02	0.02	0.02
$\Sigma REE_{(N)}$	1320	234	224	835	274	202	175	10.64	41.73	32.28	12.82	238	7626	6435	7493	192	151	509	434	314
$La_{(N)}/Lu_{(N)}$	19.46	16.36	23.20	12.56	14.88	14.35	9.71	5.46	6.72	7.54	5.82	14.43	2.35	2.50	2.42	6.36	5.59	11.01	12.20	6.61
$Eu_{(N)}/Eu*_{(N)}$	0.95	0.87	1.05	0.92	0.97	0.92	0.87	1.17	0.64	1.04	0.70	0.88	1.01	0.94	1.02	0.99	0.91	0.83	0.90	0.89

-: below detection limits (bdl).

(c)

Sample	BR2E2.6	BR2E2.7	BR2E2.8	BR2E2.9	BR2E2.10	BR2E3.1	BR2E3.2	BR2E3.3	BR2E3.4	BR2E3.5	BR2E3.6	BR2E3.7	BR2E3.8	BR2E3.9	BR2E3.10	BR6A.1	BR6A.2	BR6A.3	BR6A.4	BR6A.5	BR6A.6
P (ppm)	-	15.30	-	-	12.10	23.40	29.40	32.20	53.40	25.10	33.90	50.00	24.60	40.10	30.20	45.30	54.70	52.00	47.80	50.70	40.70
K	2.36	11.10	-	3.78	8.50	14.90	11.30	18.60	117	28.30	-	9.10	4.50	4.30	18.10	-	1.99	3.33	1.95	1.63	1.69
Sc	4.04	5.82	4.27	5.52	3.21	1.04	1.52	2.18	3.60	1.78	2.24	6.37	1.91	3.68	2.26	3.17	4.21	1.68	2.58	4.83	0.68
Ti	0.19	0.45	2.00	10.60	2.60	5.90	2.56	6.00	22.00	4.20	4.20	7.30	1.90	3.70	5.60	2.22	4.60	3.11	3.15	2.82	2.72
V	1.31	4.87	1.79	5.04	4.04	4.96	6.12	10.68	38.60	12.00	7.79	13.90	4.24	6.34	6.65	9.83	23.10	20.20	26.45	15.67	6.60
Cr	-	2.05	0.94	2.24	1.44	0.73	0.78	1.16	1.74	-	-	-	-	-	-	-	-	-	-	-	-
Mn	608	738	644	759	695	830	919	1156	2140	1110	1804	2410	1052	1866	1510	1040	1270	1016	1168	1151	902
Co	0.01	0.09	0.02	0.07	0.07	0.18	0.24	0.42	7.11	0.42	2.95	5.20	1.07	3.72	1.84	0.19	0.12	0.24	0.23	0.12	0.16
Ni	-	0.21	-	0.21	0.23	0.59	0.64	1.75	23.00	1.63	8.71	17.30	4.10	11.60	4.34	0.41	0.24	0.39	0.29	0.24	0.21
Cu	-	0.49	0.09	-	5.03	0.35	1.10	0.27	6.00	4.22	0.54	1.38	1.97	1.00	7.10	-	-	-	-	-	-
Zn	1.39	8.90	1.74	6.23	8.86	18.00	20.20	38.50	171	26.00	125	205	47.80	144	66.50	12.07	18.80	14.80	20.20	12.40	13.00
Ga	0.09	0.18	0.12	0.19	0.19	0.77	0.78	1.19	4.58	0.92	0.49	0.91	0.15	0.39	0.36	0.10	0.20	0.15	0.23	0.28	0.07
Rb	-	0.05	-	-	-	-	-	0.03	0.32	0.06	0.00	-	-	-	-	-	-	-	-	-	-
Sr	2468	2224	2310	2619	2884	1730	1791	1853	1758	1771	2032	2082	1433	1815	1988	523	1836	1067	2391	1968	736
Y	14.39	26.90	20.80	27.06	19.80	31.20	44.50	55.20	67.00	51.10	31.82	74.50	17.10	45.30	23.90	27.80	55.20	33.20	50.80	53.60	3.81
Zr	1.49	4.56	3.04	4.50	4.02	8.90	11.11	10.44	7.97	9.65	5.99	7.48	3.49	7.37	3.89	6.53	13.40	9.80	12.22	10.14	4.77
Nb	-	-	0.00	-	-	-		-	-	-	-	-	-	-	-	-	0.00	-	-	0.01	-
Cs	0.01	-	-	-	0.02	-	-		0.15	-	-	-	-	-	-	-	-	-	-	-	-
Ba	62.10	103	71.90	94.30	81.10	99.50	105	116	129	109	52.50	46.90	17.10	46.00	53.10	13.18	49.20	27.00	63.60	61.00	20.60
La	6.75	15.95	10.80	16.57	11.00	15.53	22.84	30.00	35.00	25.70	9.99	32.30	5.60	14.66	8.46	2.91	13.10	10.70	19.20	17.80	1.59
Ce	12.66	26.40	18.60	26.80	17.40	22.80	34.69	45.50	54.50	45.30	15.41	54.00	9.20	25.50	13.99	4.81	22.20	18.00	32.50	30.70	2.68
Pr	1.67	3.04	2.29	3.19	2.13	2.73	4.04	5.26	6.23	4.58	2.10	6.48	1.19	3.29	1.65	0.70	3.19	2.48	4.18	3.81	0.30
Nd	7.77	13.97	10.00	14.20	9.71	12.33	18.80	23.90	29.70	22.90	9.66	30.40	4.87	15.70	8.20	4.09	15.90	13.20	20.90	19.00	1.34
Sm	1.87	3.02	2.75	2.84	2.15	2.77	3.94	5.11	6.88	4.81	2.34	6.40	1.01	3.54	1.91	1.06	4.13	3.40	5.07	4.76	0.21
Eu	0.57	1.04	0.79	1.08	0.71	1.01	1.40	1.76	2.32	1.69	0.77	2.31	0.36	1.15	0.63	0.45	1.32	1.05	1.66	1.43	0.10
Gd	1.95	3.34	2.68	3.68	2.65	3.92	5.60	6.66	8.24	6.19	2.93	9.40	1.61	4.84	2.70	2.03	5.70	4.22	6.51	5.93	0.40
Tb	0.35	0.65	0.43	0.57	0.41	0.65	0.83	1.07	1.46	0.96	0.45	1.54	0.21	0.69	0.38	0.33	0.95	0.63	0.96	0.95	0.05
Dy	2.15	3.77	3.06	3.73	2.75	3.97	6.27	7.20	9.65	6.84	3.17	11.02	1.55	5.15	2.72	2.32	6.56	4.38	6.73	6.54	0.41
Ho	0.45	0.83	0.62	0.79	0.60	0.88	1.28	1.54	2.13	1.44	0.73	2.49	0.33	1.13	0.60	0.58	1.45	0.96	1.53	1.45	0.10
Er	1.25	2.22	1.69	2.10	1.47	2.47	3.58	4.28	5.27	3.90	2.07	7.18	1.14	3.12	1.60	1.63	4.01	2.48	3.89	3.96	0.28

Table 1: Continued.

Sample	BR2E2.6	BR2E2.7	BR2E2.8	BR2E2.9	BR2E2.10	BR2E3.1	BR2E3.2	BR2E3.3	BR2E3.4	BR2E3.5	BR2E3.6	BR2E3.7	BR2E3.8	BR2E3.9	BR2E3.10	BR6A.1	BR6A.2	BR6A.3	BR6A.4	BR6A.5	BR6A.6
Tm	0.18	0.28	0.24	0.29	0.21	0.34	0.47	0.55	0.77	0.50	0.32	0.94	0.18	0.46	0.24	0.22	0.57	0.34	0.51	0.57	0.04
Yb	1.10	1.69	1.35	1.74	1.33	1.95	2.78	3.57	4.47	3.29	1.95	5.74	1.25	3.14	1.58	1.47	3.44	2.21	2.92	3.40	0.20
Lu	0.13	0.20	0.17	0.23	0.14	0.23	0.37	0.41	0.56	0.36	0.23	0.69	0.17	0.32	0.21	0.20	0.44	0.29	0.39	0.45	0.04
Hf	-	0.11	0.01	0.05	0.07	0.13	0.19	0.22	0.13	0.10	0.09	0.06	0.02	0.08	0.08	0.10	0.22	0.11	0.13	0.17	0.06
Ta	-	-	-	-	-	-	-	-	-	0.00	-	-	-	-	0.00	-	-	-			-
Pb	1.80	5.00	2.38	4.50	6.24	8.70	10.19	14.43	38.60	17.80	47.90	47.60	21.50	57.70	31.30	18.10	35.00	31.40	45.50	31.00	9.37
Th	0.87	0.91	0.71	1.31	0.68	0.23	0.37	0.20	0.84	0.56	0.34	2.69	0.49	3.78	0.47	0.08	0.23	0.08	0.25	1.78	0.08
U	0.01	0.03	0.01	0.02	0.03	0.34	0.46	0.44	0.83	0.20	11.33	20.92	12.92	26.73	9.73	0.14	0.48	0.20	0.40	0.30	0.08
$\Sigma REE_{(N)}$	167	315	235	320	220	310	453	572	716	525	236	755	128	365	198	124	397	293	472	451	32.66
$La_{(N)}/Lu_{(N)}$	5.40	8.59	6.93	7.59	8.42	7.36	6.58	7.94	6.75	7.65	4.58	5.05	3.53	4.93	4.38	1.54	3.21	4.02	5.28	4.21	4.48
$Eu_{(N)}/Eu*_{(N)}$	0.92	1.00	0.89	1.02	0.91	0.94	0.91	0.92	0.94	0.95	0.90	0.91	0.87	0.85	0.85	0.94	0.83	0.85	0.88	0.82	1.10

-: below detection limits (bdl).

(d)

Sample	BR6A.7	BR6A.8	BR6A.9	BR6A.10	BR6A.12	BR6A.13	BR6A.14	BR6A.15	BR6A.16	BR6A.17	BR6A.18	BR6A.19	BR6A.20	BR62 - 1	BR62 - 2	BR62 - 3	BR62 - 4	BR62 - 5	BR62 - 6	BR62 - 7	BR62 - 11
P (ppm)	42.30	53.30	86.60	31.40	41.00	68.00	40.00	12.90	31.80	28.60	31.70	30.70	31.70	9.60	8.10	9.40	31.00	22.10	25.70	42.00	32.00
K	-	2.59	-	-	164	226	260	214	0.65	0.94	0.86	1.14	5.90	16.60	9.00	6.19	68.00	122	130	203	103
Sc	0.74	2.96	1.93	1.92	15.49	38.70	12.13	2.00	0.10	0.03	0.60	0.04	5.50	0.27	0.35	2.59	1.54	2.81	7.02	4.81	1.07
Ti	1.51	4.17	1.59	2.13	5.30	13.80	460	19.00	0.86	0.93	1.79	0.85	1.51	0.85	3.00	0.28	0.84	2.50	19.40	37.00	13.00
V	22.30	21.57	73.20	8.70	15.20	21.74	14.20	7.65	0.68	0.39	1.30	0.52	3.43	2.42	1.88	3.02	5.37	10.86	5.81	11.55	2.77
Cr	-	-	-	-	1.02	2.24	2.50	0.99	0.21	-	0.19	-	0.25	-	-	-	-	-	0.75	1.95	-
Mn	1071	1112	1460	1133	844	1511	759	746	1358	673	1146	1145	1236	805	854	1231	766	884	583	885	850
Co	0.15	0.25	0.21	0.08	0.43	3.02	0.64	0.05	0.06	0.03	0.16	0.06	0.05	0.02	0.04	0.09	0.05	0.05	0.10	1.62	0.11
Ni	0.23	0.36	0.35	0.32	0.94	2.18	0.57	0.13	0.16	0.04	0.28	0.07	0.13	-	0.10	0.15	0.11	0.12	0.36	2.60	0.43
Cu		0.17	-	-	0.30	1.50	2.20	0.10	0.03	0.07	-	0.05	0.29	0.28	0.15	0.18	0.47	0.21	0.59	0.61	0.73
Zn	7.76	17.50	8.77	35.20	12.80	35.20	12.70	6.12	8.95	3.24	10.10	5.17	7.73	1.67	2.93	10.00	2.91	5.67	7.40	16.40	16.70
Ga	0.22	0.20	1.32	0.12	1.77	3.45	3.05	0.70	0.05	0.02	0.06	0.02	0.16	0.05	0.10	0.19	0.42	0.82	1.27	1.86	0.95
Rb	-		-	-	0.61	0.73	1.22	0.55	-	-	-	-	0.01	0.06	0.03	-	0.31	0.42	0.52	0.88	0.35
Sr	1450	1657	500	3840	1913	2657	1220	1918	543	728	728	596	1147	1858	1792	1521	1724	1781	1224	1154	1583
Y	66.50	43.90	156	21.80	212	154	240	38.60	3.47	4.38	6.50	2.55	48.60	15.20	25.30	37.70	41.70	114	120	97.70	67.20
Zr	14.71	12.55	58.50	6.24	3.73	4.09	2.81	0.53	1.58	1.46	3.47	2.05	9.59	0.92	0.44	3.47	0.41	2.25	0.32	5.80	2.14
Nb	-	-	-	-	0.00	0.02	0.64	0.01	0.00	0.00	0.00	-	-	-	-	-	-	0.00	0.05	0.04	0.01
Cs	-	-	-	-	0.08	0.17	0.28	0.10	-	0.00	-	-	-	0.02	0.01	0.01	0.08	0.11	0.14	0.29	0.06
Ba	28.10	39.90	14.30	76.90	161	223	62.30	129	11.46	17.40	17.27	11.22	23.10	225	184	79.90	217	240	139	154	66.60
La	18.60	14.53	111	6.62	118	204	172	11.80	0.31	0.19	1.01	0.23	9.70	4.40	7.96	15.00	9.29	30.20	40.90	57.00	31.90
Ce	27.70	24.40	183	11.90	179	339	306	20.50	0.42	0.25	1.63	0.35	18.18	7.11	12.04	25.50	15.83	51.90	70.50	95.40	75.30
Pr	3.83	3.11	22.23	1.45	22.00	40.60	38.30	2.71	0.07	0.04	0.25	0.06	2.74	0.84	1.51	3.18	2.15	6.88	10.29	11.82	10.08
Nd	21.90	15.16	103	7.47	100	172	220	13.51	0.34	0.24	1.37	0.41	14.56	4.25	7.62	16.10	11.93	35.50	57.00	58.40	47.60
Sm	6.13	3.91	23.20	2.03	22.50	33.90	37.52	3.24	0.09	0.08	0.35	0.14	4.23	1.10	1.93	3.94	3.37	9.60	15.36	12.44	11.10
Eu	1.92	1.31	6.92	0.59	7.20	9.49	12.19	1.01	0.03	0.04	0.14	0.06	1.39	0.37	0.59	1.25	1.11	2.89	4.63	3.56	2.86

Table 1: Continued.

Sample	BR6A.7	BR6A.8	BR6A.9	BR6A.10	BR6A.12	BR6A.13	BR6A.14	BR6A.15	BR6A.16	BR6A.17	BR6A.18	BR6A.19	BR6A.20	BR62 - 1	BR62 - 2	BR62 - 3	BR62 - 4	BR62 - 5	BR62 - 6	BR62 - 7	BR62 - 11
Gd	8.23	4.76	25.81	2.42	27.80	30.50	41.30	3.93	0.20	0.17	0.53	0.22	5.82	1.45	2.57	5.13	4.33	12.90	18.77	14.70	10.20
Tb	1.19	0.77	3.95	0.45	4.26	4.71	5.96	0.60	0.03	0.03	0.09	0.03	0.97	0.25	0.34	0.76	0.64	1.86	2.71	2.27	1.38
Dy	7.89	5.42	25.79	2.76	26.53	28.12	36.50	3.81	0.20	0.37	0.63	0.24	6.57	1.42	2.51	5.35	4.34	12.50	16.31	13.28	8.02
Ho	1.74	1.24	5.31	0.63	5.73	5.69	6.82	0.87	0.05	0.10	0.14	0.05	1.36	0.32	0.51	1.05	0.99	2.57	3.27	2.67	1.61
Er	4.60	3.43	14.33	1.87	15.35	14.18	17.50	2.17	0.15	0.29	0.38	0.11	3.81	0.84	1.35	2.86	2.69	7.06	8.77	6.99	4.01
Tm	0.63	0.45	1.89	0.25	2.22	1.88	2.50	0.29	0.02	0.05	0.06	0.02	0.55	0.11	0.17	0.43	0.38	1.03	1.29	0.97	0.61
Yb	3.43	3.23	10.02	1.36	13.80	11.41	15.09	1.79	0.15	0.28	0.43	0.13	3.99	0.55	0.97	2.37	2.12	6.24	9.18	5.53	3.57
Lu	0.41	0.36	1.21	0.15	1.70	1.32	1.86	0.26	0.02	0.03	0.05	0.01	0.48	0.09	0.12	0.28	0.28	0.79	1.15	0.70	0.39
Hf	0.15	0.21	0.75	0.08	0.04	0.07	-	0.00	0.03	0.03	0.06	0.04	0.10	-	-	0.06	-	0.03	0.02	0.20	0.04
Ta	-	-	-	-	0.00	0.00	0.09	0.00	-	-	-	-	-	-	-	-	-	-	0.00	0.00	0.00
Pb	67.20	27.88	88.90	15.20	9.50	19.41	6.00	3.40	3.01	1.08	7.70	6.42	6.02	2.03	1.95	11.42	2.77	11.45	3.10	3.20	7.59
Th	0.03	0.17	0.06	0.64	3.47	7.53	1.30	0.64	0.01	-	0.01	0.00	1.45	0.14	0.18	0.49	0.17	0.71	0.38	0.81	17.20
U	0.10	0.39	0.14	0.68	1.39	1.97	1.33	0.79	2.76	0.66	0.78	1.16	0.58	0.12	0.26	0.34	0.35	1.08	0.86	1.84	0.55
$\Sigma REE_{(N)}$	506	373	2186	183	516	2290	3359	3546	290	11.37	14.84	36.34	11.03	374	103	174	364	282	831	1187	1161
$La_{(N)}/Lu_{(N)}$	4.86	4.28	9.81	4.64	5.65	7.45	16.58	9.91	4.90	1.85	0.58	2.08	2.08	2.15	5.55	7.11	5.70	3.52	4.08	3.82	8.68
$Eu_{(N)}/Eu*_{(N)}$	0.83	0.93	0.86	0.81	0.85	0.88	0.90	0.95	0.87	0.78	0.94	0.96	0.98	0.86	0.88	0.81	0.85	0.89	0.79	0.83	0.80

-: below detection limits (bdl).

Table 2: Whole-rock major and trace element geochemistry of greyschist, altered greyschist, and hydrothermal breccia from Bruce Rocks.

Lithology	Greyschist			Altered greyschist				Hydrothermal breccia	
Sample	BRWR-1	BRWR-2	BRWR-3	BRWR-4A	BRWR-4B	BRWR-5	BRWR-6	BRWR-7	BRWR-8
SiO_2 (wt.%)	67.94	64.57	69.86	40.85	41.73	53.09	49.00	40.74	37.93
TiO_2	0.79	0.78	0.59	0.45	0.59	0.39	0.65	0.44	0.25
Al_2O_3	16.23	17.35	13.40	8.57	11.06	9.76	12.34	9.54	6.20
Fe_2O_3	3.00	3.54	3.33	7.60	7.05	4.00	5.14	4.74	3.86
CaO	0.43	0.75	1.30	15.50	13.85	10.85	10.10	18.60	22.90
MgO	1.12	1.38	1.17	3.43	3.10	2.96	2.78	2.03	2.58
MnO	0.04	0.05	0.05	0.14	0.13	0.08	0.11	0.20	0.33
Na_2O	3.63	4.06	3.91	2.23	2.91	3.01	3.54	2.67	0.33
K_2O	2.72	2.88	1.72	1.12	1.48	1.32	1.72	1.17	1.88
LOI	3.75	4.37	4.26	19.02	17.18	13.67	13.14	18.90	22.32
Total	99.65	99.73	99.59	98.91	99.08	99.13	98.52	99.03	98.58
Ba (ppm)	662	686	392	292	363	340	437	280	555
Ce	38	45	40	52	45	25	35	23	29
Cr	20	20	10	10	10	10	20	10	20
Cs	3.28	3.30	1.95	1.37	1.61	1.66	2.17	3.51	6.20
Dy	2.64	2.80	2.70	8.28	6.72	4.30	4.09	3.16	2.85
Er	1.72	1.61	1.40	4.84	4.01	2.72	2.55	2.22	1.78
Eu	0.91	1.13	1.11	2.04	1.65	1.04	1.14	0.77	0.53
Ga	21	21	15	11	13	11	15	10	8.70
Gd	3.03	3.49	3.33	7.28	5.81	3.75	3.82	2.77	2.74
Hf	6.30	5.50	4.30	2.80	3.70	3.00	4.10	3.00	2.10
Ho	0.57	0.56	0.48	1.74	1.40	0.96	0.86	0.74	0.61
La	18	21	19	28	24	14	18	13	14
Lu	0.26	0.23	0.19	0.56	0.42	0.34	0.34	0.23	0.26
Nb	7.60	7.50	5.30	3.80	4.90	3.40	5.10	3.60	4.50
Nd	18	21	20	27	23	13	17	12	13
Pr	4.60	5.32	4.98	6.54	5.45	2.93	4.10	2.74	3.16
Rb	94	97	55	38	47	45	59	36	73
Sm	3.33	4.22	3.83	5.91	5.24	2.86	3.44	2.41	2.60
Sn	2.00	2.00	1.00	1.00	1.00	1.00	2.00	1.00	1.00
Sr	43	63	93	652	563	469	364	296	350
Ta	0.60	0.60	0.40	0.30	0.40	0.30	0.40	0.30	0.30
Tb	0.41	0.50	0.48	1.16	0.99	0.65	0.64	0.43	0.45
Th	8.59	9.10	6.99	4.48	4.90	3.71	5.34	3.96	5.60
Tm	0.26	0.22	0.18	0.66	0.52	0.43	0.36	0.27	0.27
U	1.43	1.81	1.38	1.33	1.14	1.49	0.90	0.60	1.95
V	105	100	75	66	80	52	85	57	53
W	2.00	2.00	2.00	1.00	2.00	2.00	1.00	1.00	1.00
Y	15	14	13	53	43	34	30	27	28
Yb	1.80	1.74	1.42	4.15	3.27	2.49	2.29	1.64	1.73
Zr	233	200	150	103	137	119	167	117	76

The outcrop is cut by a fault that contains a 1.5-meter-thick layer of carbonate-cemented breccia surrounded by a 0.1–1 m wide carbonate-bearing alteration zone (Figure 7(a)). Three samples represent the greyschist host rocks (samples 1, 2, and 3); two samples were collected from within the main alteration zone (sample 5 from the margin and sample 6 closer to the fault breccia); two samples were collected from within a subsidiary 20 cm-thick alteration zone surrounding a hydrothermal vein lying parallel to the foliation (samples 4A and 4B); and two samples were collected from the fault breccia (samples 7 and 8).

Whole-rock SiO_2 values of the greyschist range from 65 to 70 wt.%, with CaO, Fe_2O_3, and MgO between 1 and 4 wt.% (Table 2). The greyschist in the alteration zone,

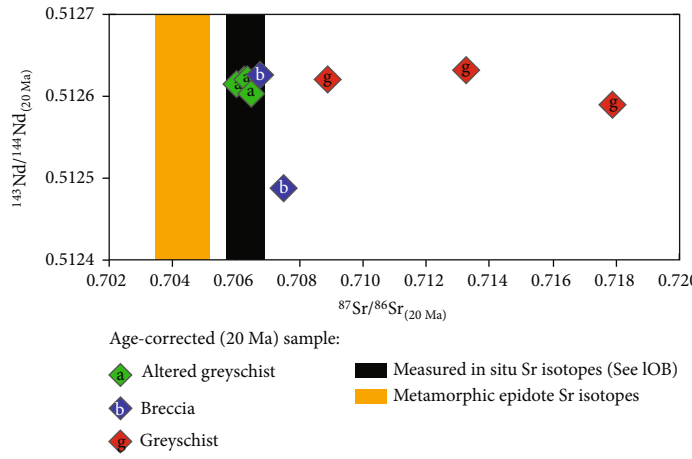

(a)

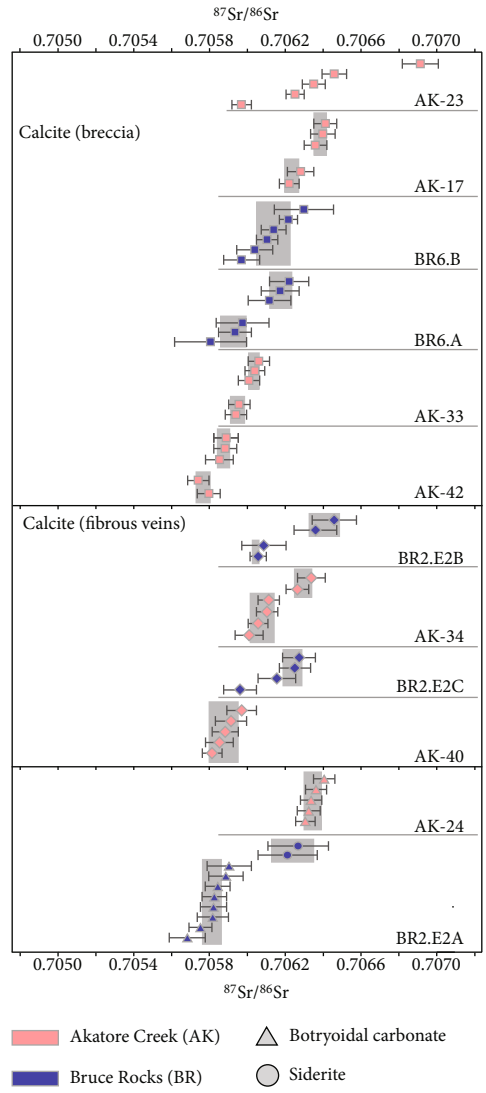

(b)

Figure 8: Strontium and neodymium isotopes. (a) Measured in situ $^{87}Sr/^{86}Sr$ of carbonate phases (the grey area, see (b) for data) compared to age-corrected (20 Ma) measured whole-rock $^{87}Sr/^{86}Sr$ and $^{143}Nd/^{144}Nd$ from the greyschist, altered greyschist, and hydrothermal breccia. Published in-situ $^{87}Sr/^{86}Sr$ for epidote are plotted for comparison [11, 24]. (b) Individual in situ $^{87}Sr/^{86}Sr$ isotope data of the different types of carbonate phases from Akatore Creek and Bruce Rocks. The grey boxes represent the weighted average Sr isotope ratio with errors from each group of samples.

Table 3: Whole-rock Sr-Nd isotope ratios (±2σ errors), including age correction to 20 Ma to represent a Miocene age.

Sample	Rb (ppm)	Sr (ppm)	Sm (ppm)	Nd (ppm)	$^{87}Sr/^{86}Sr$	±2σ	$^{87}Sr/^{86}Sr$ (20 ma)	±2σ	$^{143}Nd/^{144}Nd$	±2σ	ϵ_{Nd} (20 ma)	$^{143}Nd/^{144}Nd$ (20 ma)	±2σ
BRWR-1	93.5	42.7	3.33	18.1	0.71917	0.000014	0.71791	0.000014	0.51260	0.000009	-0.43	0.51259	0.000009
BRWR-2	96.8	63	4.22	21.4	0.71455	0.000017	0.71328	0.000017	0.51265	0.000012	0.41	0.51263	0.000012
BRWR-3	55.3	92.9	3.83	19.6	0.70939	0.000013	0.70890	0.000013	0.51264	0.000010	0.19	0.51262	0.000010
BRWR-4A	37.6	652	5.91	26.6	0.70639	0.000015	0.70634	0.000015	0.51262	0.000012	-0.15	0.51260	0.000012
BRWR-4B	47.4	563	5.24	22.5	0.70662	0.000011	0.70655	0.000011	0.51264	0.000010	0.17	0.51262	0.000010
BRWR-5	44.6	469	2.86	13	0.70649	0.000021	0.70641	0.000021	0.51264	0.000011	0.17	0.51262	0.000011
BRWR-6	58.8	364	3.44	16.8	0.70696	0.000011	0.70636	0.000011	0.51263	0.000010	0.06	0.51262	0.000010
BRWR-7	36.2	296	2.41	11.6	0.70689	0.000013	0.70679	0.000013	0.51264	0.000011	0.29	0.51263	0.000011
BRWR-8	73.4	350	2.6	12.6	0.70769	0.000012	0.70751	0.000012	0.51250	0.000010	-2.42	0.51249	0.000010

Table 4: In situ average $^{87}Sr/^{86}Sr$ isotope ratios with error and mean square weighted deviation (MSWD) values from the different carbonate types.

Locality	Sample	Lithology	$^{87}Sr/^{86}Sr$	$\pm 2\sigma$	No.	MSWD
Akatore Creek	AK17-1	Breccia	0.70624	0.00039	2	2.1
	AK17-2	Breccia	0.70639	0.00004	3	0.7
	AK23-1	Breccia	0.70635	0.00006	1	—
	AK23-2	Breccia	0.70692	0.00010	1	—
	AK23-3	Breccia	0.70646	0.00007	1	—
	AK23-4	Breccia	0.70626	0.00005	1	—
	AK23-5	Breccia	0.70598	0.00005	1	—
	AK24	Botryoidal carbonate	0.70633	0.00005	5	2
	AK33-1	Breccia	0.70595	0.00004	2	0.2
	AK33-2	Breccia	0.70604	0.00003	3	0.74
	AK34-1	Fibrous vein	0.70630	0.00047	2	2.5
	AK34-2	Fibrous vein	0.70608	0.00007	4	2.1
	AK40	Fibrous vein	0.70588	0.00008	5	3.2
	AK42-1	Quartz-calcite vein	0.70577	0.00037	2	2.1
	AK42-2	Quartz-calcite vein	0.70588	0.00004	3	0.29
Bruce rocks	BR2.E2A-1	Botryoidal carbonate	0.70579	0.00005	8	2.6
	BR2.E2A-2	Siderite	0.70624	0.00011	2	0.25
	BR2.E2B-1	Fibrous vein	0.70641	0.00008	2	1.5
	BR2.E2B-2	Fibrous vein	0.70606	0.00004	2	0.28
	BR2.E2C-1	Fibrous vein	0.70596	0.00009	1	—
	BR2.E2C-2	Fibrous vein	0.70624	0.00005	3	1.9
	BR6.A-1	Breccia	0.70593	0.00007	3	1.1
	BR6.A-2	Breccia	0.70618	0.00059	3	0.98
	BR6.B	Quartz-calcite vein	0.70614	0.00009	6	6.3

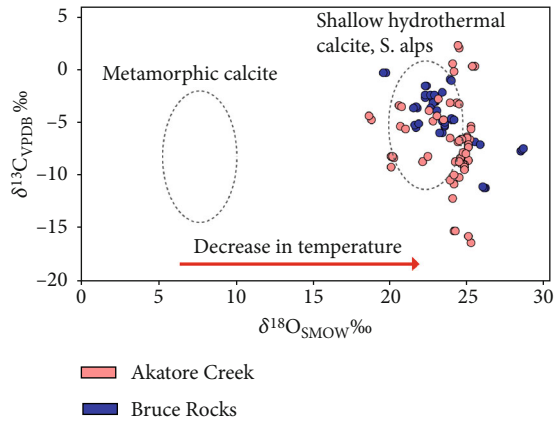

Figure 9: $\delta\ ^{13}C_{VPDB}$ ‰ and $\delta^{18}O_{SMOW}$ ‰ of carbonates from Akatore Creek and Bruce Rocks, compared with the fields for primary metamorphic calcite and shallow hydrothermal calcite in the Southern Alps of New Zealand [10]. Remobilisation and recrystallisation of metamorphic calcite and precipitation at a lower temperature are interpreted to have caused an increase in $\delta^{18}O_{SMOW}$ ‰ (indicated by arrow).

however, has lower SiO_2 = 40–50 wt.% and higher CaO (10–15 wt.%), Fe_2O_3, and MgO (3–7 wt.%) (Table 2). The fault breccia also has low SiO_2 (37–40 wt.%) and high CaO (18–22 wt.%) (Table 2). Loss on ignition (LOI) and Sr are both low in the greyschist samples (LOI = 3–4 wt.%, Sr = 42.7–92.9 ppm; Table 2), but distinctly higher in the altered greyschist (LOI = 13–17 wt.%, Sr = 364-652) and the fault breccia (LOI = 18–22 wt.%, Sr = 296–350 ppm; Table 2).

Mass balance calculations show losses and gains of major and trace elements during alteration (Figure 7(b)). Volume corrections were applied by calculating a correction factor (k) according to the abundances of TiO_2, Zr, Nb, and Hf, which appear to have been immobile during alteration [11]. Each element from the altered samples was compared to the average of the unaltered greyschist (samples 1-3; Figure 7). Results suggest that during alteration there was enrichment in CaO, Fe_2O_3, MgO, MnO, Sr, and Y, as well as several REEs, with small losses in SiO_2, Al_2O_3, and K_2O (Figure 7).

4.6. Strontium and Neodymium Isotopes. Whole-rock $^{143}Nd/^{144}Nd$ isotope ratios of the greyschist (samples 1-3: $^{143}Nd/^{144}Nd$ = 0.51260–0.51265), altered greyschist (samples 4-6: $^{143}Nd/^{144}Nd$ = 0.51250–0.51264) and the fault breccia (samples 7-8: $^{143}Nd/^{144}Nd$ = 0.51262–0.51264) cluster around $^{143}Nd/^{144}Nd$ = 0.5126 (Figure 8(a)), with the exception of one fault breccia sample that is less radiogenic (sample 8: $^{143}Nd/^{144}Nd$ = 0.51249; Figure 8(a), Table 3).

Table 5: Calculated $\delta^{13}C_{VPDB}$‰ and $\delta^{18}O_{SMOW}$‰ stable isotope ratios of hydrothermal carbonate phases from Akatore Creek and Bruce Rocks.

Sample	$\delta^{13}C_{VPDB}$ (‰)	$\delta^{18}O_{SMOW}$ (‰)
AK14-A	-8.05	20.24
AK14-B	-9.15	20.13
AK15-A	-6.78	24.50
AK15-B	-6.34	23.95
AK16-A	-8.63	24.32
AK16-B	-8.65	24.54
AK17-A	-10.68	24.21
AK17-B	-10.28	23.93
AK18-A	-6.92	25.11
AK18-B	-7.20	25.11
AK21-A	-8.86	24.85
AK21-B	-8.80	24.77
AK23-A	-9.06	24.87
AK23-B	-9.32	24.85
AK24-A	-5.18	20.74
AK24-B	-5.43	21.04
AK26A-A	-6.25	25.09
AK26A-B	-6.45	25.20
AK26B-A	-3.70	22.61
AK26B-B	-4.69	22.89
AK26C-A	-3.23	20.60
AK26C-B	-3.40	20.85
AK28-A	-2.96	24.39
AK28-B	-3.06	24.58
AK30-A	-6.51	24.73
AK30-B	-6.55	24.56
AK31-A	0.46	25.56
AK31-B	0.53	25.43
AK33-A	-3.05	23.97
AK33-B	-2.68	23.21
AK34-A	2.18	24.57
AK34-B	2.47	24.47
AK37-A	-6.36	25.06
AK37-B	-6.45	24.63
AK38-A	-4.27	23.10
AK38-B	-4.63	23.54
AK39-A	0.04	24.23
AK39-B	0.79	24.09
AK40-A	-4.62	18.88
AK40-B	-4.20	18.68
AK41-A	-16.32	25.31
AK41-B	-15.71	25.18
AK42-A	-15.23	24.17
AK42-B	-15.19	24.27
AK43A-A	-5.19	25.35
AK43A-B	-5.53	25.28
AK43B-A	-8.25	24.60
AK43B-B	-8.69	24.60
AK46-A	-12.11	24.10
AK46-B	-12.07	24.11
AK49-A	-7.78	24.82
AK49-B	-7.82	25.00
AK4A-A	-8.63	22.14
AK4A-B	-8.14	22.52
AK4B-A	-8.14	20.15
AK4B-B	-8.16	20.32
AK50-A	-8.39	24.73
AK50-B	-8.44	25.10
AK51-A	-10.06	24.54
AK51-B	-9.84	24.24
BR1.B V1	-5.86	23.40
BR1.B V2	-5.80	23.28
BR1.B V3	-5.87	23.26
BR13 B B1	-0.77	23.96
BR13 B B2	-0.87	24.02
BR13 B V1	-2.05	23.45
BR13.DB V1	-5.27	23.64
BR13.DB V2	-4.70	23.46
BR13.DB V3	-5.11	23.61
BR2 A B1	-11.07	26.22
BR2 A B2	-11.12	26.17
BR2 A B3	-10.91	26.11
BR2.E2 CC1A	-3.44	21.87
BR2.E2 CC1B	-3.43	21.72
BR2.E2 CC1C	-3.48	21.55
BR2.E2 CC2A	-2.81	23.02
BR2.E2 CC2B	-2.77	22.84
BR2.E2 V1	-5.33	21.78
BR2.E2 V2	-5.13	21.66
BR2.E2 V3	-5.04	21.92
BR2.E3 CC2C	-2.84	22.91
BR6 AB B1	-4.66	24.06
BR6 AB B2	-4.55	24.06
BR6 AB B3	-4.60	24.17
BR6 AF B1	-2.26	22.33
BR6 AF B2	-2.28	22.68
BR6 AF B3	-2.29	22.94
BR6 DA V2	-3.47	22.69
BR6 DA V3	-3.71	23.13
BR6 DR V1	-3.06	22.81
BR6.AC B1	-4.86	23.63
BR6.AC B2	-6.76	25.57
BR6.AC B3	-6.97	25.91
BR6.AC1 B1	-1.40	22.40
BR6.AC1 B2	-1.42	22.43

Table 5: Continued.

Sample	$\delta^{13}C_{VPDB}$ (‰)	$\delta^{18}O_{SMOW}$ (‰)
BR6.AC1 B3	-1.38	22.37
BR6.B B1	-7.57	28.52
BR6.B B2	-7.44	28.59
BR6.B B3	-7.39	28.74
BR6.B QV1	-0.10	19.80
BR6.B QV2	-0.14	19.65
BR6.B1 B1	-2.41	22.46
BR6.B1 B2	-2.45	22.35
BR6.B1 B3	-2.47	22.31

Strontium isotopes were measured on whole-rock samples (Table 3; Figure 8(a)) and in situ on vein carbonates (Table 4; Figure 8(b)). The whole-rock $^{87}Sr/^{86}Sr$ ratios show the unaltered greyschists (samples 1-3) to be more radiogenic ($^{87}Sr/^{86}Sr = 0.70939–0.71917$) than either the altered greyschist (samples 4-6: $^{87}Sr/^{86}Sr = 0.70639–0.70696$) or the fault breccias (samples 7 and 8: $^{87}Sr/^{86}Sr = 0.70689–0.70769$). In situ $^{87}Sr/^{86}Sr$ data of hydrothermal calcite and siderite from both study areas occupy a relatively narrow range of $^{87}Sr/^{86}Sr = 0.70577–0.70646$, with a majority plotting at 0.7060–0.7062 and overlapping with the hydrothermally altered whole rock analyses (Figures 8(a) and 8(b)). Botryoidal carbonate from a hydrothermal vein at Bruce Rocks, and calcite from a calcite-quartz vein at Akatore Creek, both yielded an average $^{87}Sr/^{86}Sr$~0.70578 and were the least radiogenic samples (Figure 8(b)). Siderite grains at Bruce Rocks have Sr isotope ratios of 0.70624 ± 0.00011 ($n = 2$) (Table 4; Figure 8(b)).

4.7. Carbon and Oxygen Isotopes. The $\delta^{13}C_{VPDB}$ and $\delta^{18}O_{SMOW}$ values of five calcite samples from Bruce Rocks show a range of $\delta^{13}C_{VPDB}$ from -11.to 0.8‰ and $\delta^{18}O_{SMOW}$ ranging from 21.7 to 28.6‰ (Figure 9; Table 5). A larger spread of $\delta^{13}C_{VPDB}$ (-16.0 to 2.3‰) and $\delta^{18}O_{SMOW}$ (18.8 to 25.5‰) is present in six calcite samples from Akatore Creek (Figure 9; Table 5).

5. Discussion

5.1. Structural Controls on the Shallow Hydrothermal Fluid System. We interpret the paleohydrothermal systems exposed at Akatore Creek and Bruce Rocks to have developed within the Otago Schist under low-temperature and low-pressure conditions (Figure 10). The presence of infrequent thin (type 1) deformation twins in calcite suggests temperatures below 170°C [50, 52, 53]. Additionally, the range of $\delta^{13}C$ and $\delta^{18}O$ values overlaps with other datasets obtained from shallow (<5 km depth; [10]) cavity-filling hydrothermal vein calcite in the Southern Alps of New Zealand [10] (Figures 9 and 10). This field of $\delta^{13}C$ and $\delta^{18}O$ has previously been interpreted to represent remobilisation of metamorphic calcite and reprecipitation at low temperatures (200-300°C; [10]). Primary metamorphic calcite in the Otago Schist makes up c. 5% of the modal mineralogy, and has a restricted carbon and oxygen stable isotope range, where relatively low $\delta^{13}C$ likely reflects metamorphism of primary organic matter (Figure 9, [10, 54, 55]). Breakdown of metamorphic carbonate and liberation of CO_2 into a relatively shallow hydrothermal system will result in fluid precipitation at a lower temperature, and therefore a shift towards higher $\delta^{18}O$ values while maintaining an overlap in $\delta^{13}C$ values (Figure 9, [10]). Overall, the carbon and oxygen isotope ratios from both study areas are clustered and overlap with published data collected from carbonates that were precipitated in shallow hydrothermal systems in the Southern Alps [10, 11].

Structural observations suggest that on a macroscale (metres to decametres) fluid flow was strongly channelized along foliation surfaces and Cretaceous exhumation joints that were reactivated as small-displacement strike-slip faults. This formed breccia- and vein-bearing fault networks with orientations that were strongly controlled by the orientations of the preexisting joint sets (Figure 10(a)). On a more local scale, fluid diffusion from the faults into the surrounding wall rocks was controlled mainly by the permeability of the schist wall rocks, which favoured fluid penetration along foliation surfaces and grain boundaries (Figure 10(b)). Additionally, large volumes of fluid appear to have been channelled within dilational jogs connecting overlapping fault segments, a geometry that was likely inherited from overlapping joints (Figures 4(c), 4(e), and 4(g)). Since the fault networks (and associated breccias and veins) are the youngest tectonic structures observed in the field areas, this supports the interpretation that faulting and associated hydrothermal fluid flow occurred under relatively low-temperature conditions, since the exhumation joints are thought to have formed mainly above the ductile-to-brittle transition at <250°C [31].

The calculated paleostress tensor for the strike-slip fault networks at Akatore Creek is characterised by a σ_1 azimuth of 094° and a subvertical σ_2, representing an Andersonian strike-slip stress regime (Figure 2(g)). The modern-day stress tensor in the Otago and Canterbury regions contains a subhorizontal σ_1 with an azimuth of 115° ± 5° [39, 40] similar to the paleo-σ_1 derived from the strike-slip faults in the study areas. The contemporary stress field is thought to have initiated in the Early Miocene, when the South Island of New Zealand experienced a transition from dominantly extensional tectonics to dominantly compressional and strike-slip tectonics, controlled by the development of the Alpine Fault as the modern-day plate boundary [39]. During compressional inversion, previously formed Cretaceous–Oligocene basin-bounding normal fault systems –including the Akatore Fault in the study area– were reactivated as high-angle reverse faults that continue to be active to the present day [56]. Our interpretation is that the vein- and breccia-bearing strike-slip fault networks exposed at Akatore Creek and Bruce Rocks (Figures 2–4) represent shallowly formed, post-Early Miocene structures that formed in a stress field similar to the contemporary stress field. If this is correct, the fault networks broadly overlap in age with reverse movements on the nearby Akatore Fault, which has accumulated several hundreds of metres of reverse displacement at the surface since the Miocene [35–42, 44–57]. The fault networks exposed along the coast may therefore represent the

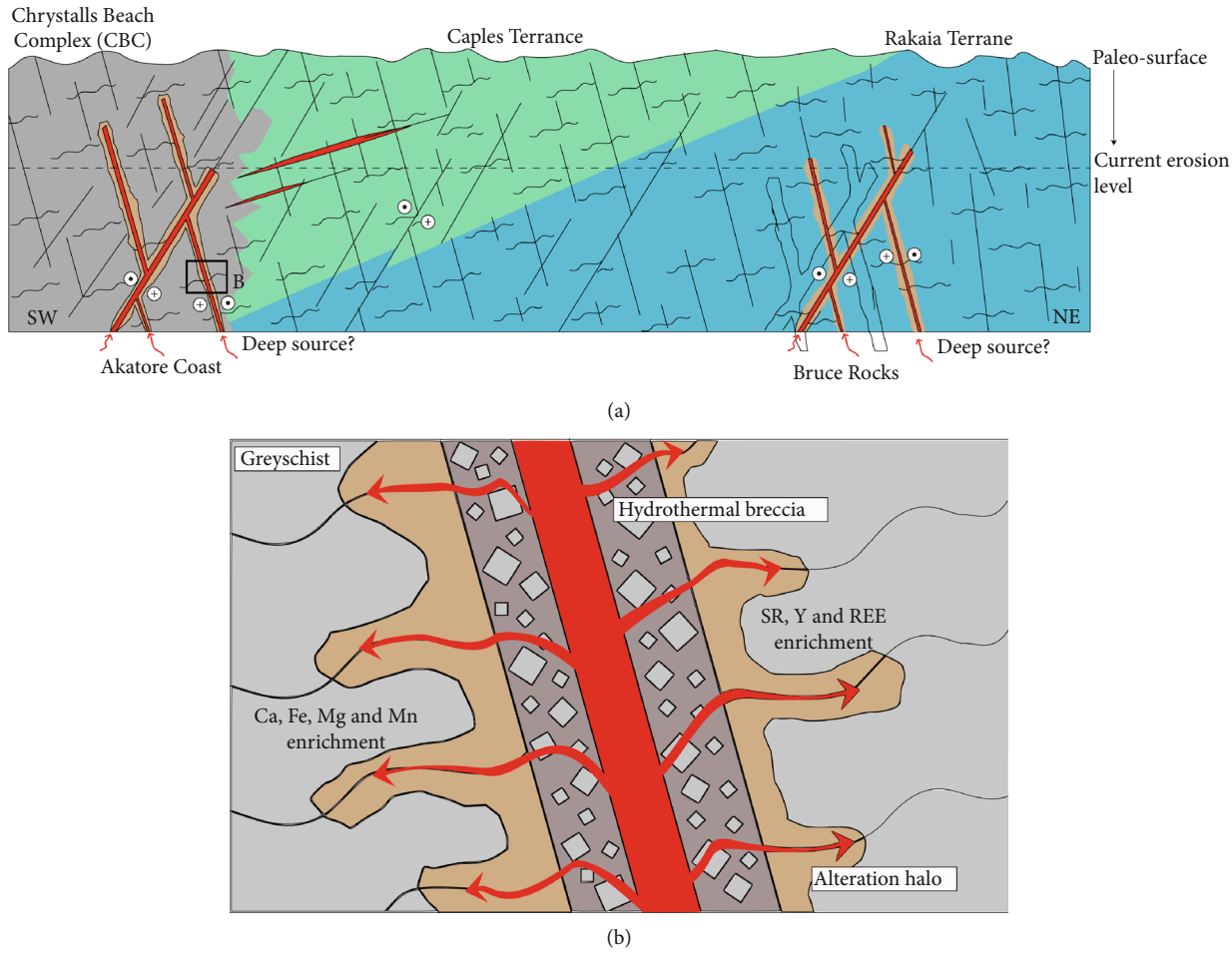

Figure 10: Cartoon interpretation of the formation of the shallow hydrothermal systems at Akatore Creek and Bruce Rocks. (a) Cross-section of the Otago Schist, showing reactivation of Late Cretaceous exhumation joints as post-Early Miocene brittle fault networks that resulted in strongly channelized shallow fluid flow. (b) Structural controls on fluid flow include preferential flow along faults (reactivated joints) and the Mesozoic foliation, causing enrichment in Ca, Fe, Mg, Mn, Sr, Y, and REE within the alteration zone.

manifestation of broadly distributed, upper-crustal deformation within the "damage zones" of regional-scale reverse faults such as the Akatore Fault. The broadly synchronous activity of steep, NE-SW striking reverse faults (e.g., Akatore Fault) and conjugate sets of strike-slip faults, is a deformation pattern similar to that recognized in recent earthquake sequences in Otago and Canterbury. For example, the 2010-2011 Canterbury earthquake sequence involved activation of steeply-dipping, NE-SW striking reverse faults and conjugate sets of E-W (dextral) and NW-SE (sinistral) trending strike-slip to oblique-slip faults, with orientations comparable to those documented in this paper [40]. Analysis of stress ratios in Otago and Canterbury suggest that the magnitude of σ_3 is similar to the magnitude of σ_2, meaning that switching between "strike-slip" and "reverse" Andersonian stress regimes is possible [40, 41]. One possibility is that the fault networks described here represent distributed deformation associated with rupture on the Akatore Fault, in which case the carbonate-cemented breccias and carbonate veins may reflect channelized fluid flow associated with permeability increases within coseismic fracture zones.

5.2. Evolution of Fluid Composition and Wall-Rock Interaction. Paleohydrothermal fluid flow was associated with enrichments in CaO, Fe_2O_3, MgO, CO_2, and MnO, and losses in SiO_2, Al_2O_3, and K_2O during alteration of the schist wall rocks (Figure 10). This mobilisation correlates with precipitation of calcite, ankerite, and siderite as the main carbonate phases. Petrographic observations of syntaxial veins showing a distinct compositional difference between the core (calcite) and rims (siderite) suggests that there was a change in fluid composition from early Fe-rich fluids to later Ca-rich (and Fe-depleted) fluids. One possible reason for this could be the late precipitation of hydrothermal pyrite that would result in the removal of Fe in the system.

Strontium is a useful trace element in hydrothermal carbonate minerals because it has a similar charge and ionic radius to Ca, which means a substitution can readily occur. Potassium, which is substituted easily by Rb, is not compatible in carbonate phases due to a much larger ionic radius than Ca, and so the carbonate Sr isotope ratio is not affected by overdecay of ^{87}Rb. Any variation of Sr isotopic compositions in hydrothermal carbonates will therefore reflect

fluid-rock interaction. The majority of in-situ Sr isotope data from the hydrothermal carbonate phases varies between $^{87}Sr/^{86}Sr = 0.70577$ and 0.70646 and shows no significant difference between the different types of carbonate texture (Figure 8, Table 4). The high Sr concentration in mica-rich layers within fibrous foliation-parallel veins is also coupled to the most radiogenic Sr isotope ratio of 0.70641 ± 0.00008 ($n = 2$). The value is lower than age-corrected (20 Ma) bulk Otago Schist ($^{87}Sr/^{86}Sr_{(20\ Ma)}$ of 0.70890–0.71791) (Figure 8(a), Table 4). Therefore, the hydrothermal carbonates require interaction between a moderately unradiogenic component and a relatively radiogenic component. The radiogenic component could be derived from breakdown of mica grains, which are hosted within the hydrothermal fault breccias and altered greyschist and have interacted with the hydrothermal carbonates. The origin of an unradiogenic Sr component requires breakdown of mineral phases that have low Rb/Sr. Metamorphic epidote is a minor component in the greyschist but has $^{87}Sr/^{86}Sr$ of 0.70343–0.70519 [11, 25] that is less radiogenic than the hydrothermal carbonates ($^{87}Sr/^{86}Sr = 0.70577$–$0.70646$; Figures 8(a) and 8(b), Table 2).

Since metamorphic epidote takes up no Rb, it is representative of the initial greyschist Sr isotope ratio at the time of Otago Schist metamorphism (150-135 Ma–Late Jurassic-Early Cretaceous; [28]). Other possibilities for non-radiogenic fluid components are metamorphic plagioclase and metamorphic calcite, both of which have low Rb/Sr and therefore should have the same initial metamorphic value as the epidote. Age correction of the Otago Schist bulk rocks gives a similar value to the metamorphic epidote. A key point is that the CO_2-rich nature of the fluids that fluxed through Bruce Rocks and Akatore Creek suggests that metamorphic carbonate was probably mobilised in the fluid source. Since the hydrothermal fault breccias have higher fluid: rock ratios than the surrounding wall-rock, this may explain why whole-rock Sr isotope data of the hydrothermal breccias are more radiogenic than the altered greyschist. Another reason could be that the hydrothermal fault breccias have a higher concentration of hydrothermal carbonate compared to the altered greyschist.

6. Conclusions

The vein- and breccia-bearing fault networks exposed at Akatore Creek and Bruce Rocks are interpreted to represent a post-Early Miocene hydrothermal system that formed at shallow depths in the Otago Schist. The orientation and geometry of the fault networks and the associated channelized fluid flow were strongly influenced by the metamorphic foliation and by reactivation of preexisting Cretaceous exhumation joints. Paleostress analysis suggests that the small-displacement strike-slip fault networks developed in a paleostress field containing a maximum principal stress (σ_1) oriented at c. 094°, which is similar to the modern-day σ_1 orientation in Canterbury and Otago. The $\delta^{18}O$ values of vein carbonates in the field areas overlap with shallow hydrothermal calcite elsewhere in the South Island. Stable isotope data coupled with the presence of thin type 1 twins in calcite implies vein precipitation under low-temperature conditions (<200°C). Sr isotope data indicate that the carbonate Sr isotope signature is inherited from mixing between an unradiogenic and a radiogenic source. The unradiogenic source may be metamorphic epidote and calcite, while the radiogenic source is likely to be muscovite from the host greyschists, although meteoric water and seawater cannot be ruled out. The brittle fault networks and associated hydrothermal systems are interpreted to have formed after the onset of Early Miocene compression, and may represent fracturing and fluid flow associated with reverse reactivation of regional-scale faults such as the nearby Akatore Fault.

Data Availability

The collected geochemical data used to support the findings of this study are included within the article.

Conflicts of Interest

The authors declare that there is no conflict of interest regarding the publication of this paper.

Acknowledgments

This research was funded by the University of Otago research grants to James M. Scott and Steven A.F. Smith and by Marsden Fund project UOO1829.

References

[1] J. Suppe, "Absolute fault and crustal strength from wedge tapers," *Geology*, vol. 35, no. 12, pp. 1127–1130, 2007.

[2] R. H. Sibson, "Crustal stress, faulting and fluid flow," *Geological Society, London, Special Publications*, vol. 78, no. 1, pp. 69–84, 1994.

[3] J. Townend and M. D. Zoback, "How faulting keeps the crust strong," *Geology*, vol. 28, no. 5, pp. 399–402, 2000.

[4] F. Ghisetti and L. Vezzani, "Normal faulting, transcrustal permeability and seismogenesis in the Apennines (Italy)," *Tectonophysics*, vol. 348, no. 1-3, pp. 155–168, 2002.

[5] R. H. Sibson, "Earthquake faulting as a structural process," *Journal of Structural Geology*, vol. 11, no. 1-2, pp. 1–14, 1989.

[6] L. Valoroso, L. Chiaraluce, C. Collettini et al., "Earthquakes and fault zone structure," *Geology*, vol. 42, no. 4, pp. 343–346, 2014.

[7] R. I. Higgins and L. B. Harris, "The effect of cover composition on extensional faulting above re-activated basement faults: results from analogue modelling," *Journal of Structural Geology*, vol. 19, no. 1, pp. 89–98, 1997.

[8] I. K. Pitcairn, D. A. H. Teagle, D. Craw, G. R. Olivo, R. Kerrich, and T. S. Brewer, "Sources of metals and fluids in orogenic gold deposits: insights from the Otago and Alpine Schists, New Zealand," *Economic Geology*, vol. 101, no. 8, pp. 1525–1546, 2006.

[9] D. Craw, P. O. Koons, T. Horton, and C. P. Chamberlain, "Tectonically driven fluid flow and gold mineralisation in active collisional orogenic belts: comparison between New Zealand and western Himalaya," *Tectonophysics*, vol. 348, no. 1-3, pp. 135–153, 2002.

[10] D. Craw, P. Upton, and D. J. Mackenzie, "Hydrothermal alteration styles in ancient and modern orogenic gold deposits,

New Zealand," *New Zealand Journal of Geology and Geophysics*, vol. 52, no. 1, pp. 11–26, 2009.

[11] A. K. Wellnitz, J. M. Scott, C. E. Martin et al., "Carbonation reactions and coupled element and isotope redistribution during shallow crustal gold mineralisation, New Zealand," *Mineralium Deposita*, vol. 54, no. 5, pp. 743–760, 2019.

[12] C. M. Breeding and J. J. Ague, "Slab-derived fluids and quartz-vein formation in an accretionary prism, Otago Schist, New Zealand," *Geology*, vol. 30, no. 6, pp. 499–502, 2002.

[13] D. Craw, M. Begbie, and D. MacKenzie, "Structural controls on Tertiary orogenic gold mineralization during initiation of a mountain belt, New Zealand," *Mineralium Deposita*, vol. 41, no. 7, pp. 645–659, 2006.

[14] N. Mortimer, P. Gans, A. Calvert, and N. Walker, "Geology and thermochronometry of the east edge of the Median Batholith (Median Tectonic Zone): a new perspective on Permian to Cretaceous crustal growth of New Zealand," *The Island Arc*, vol. 8, no. 3, pp. 404–425, 1999.

[15] J. M. Scott, "A review of the location and significance of the boundary between the Western Province and Eastern Province, New Zealand," *New Zealand Journal of Geology and Geophysics*, vol. 56, no. 4, pp. 276–293, 2013.

[16] N. Mortimer, "New Zealand's geological foundations," *Gondwana Research*, vol. 7, no. 1, pp. 261–272, 2004.

[17] R. J. Norris and A. F. Cooper, "Late Quaternary slip rates and slip partitioning on the Alpine Fault, New Zealand," *Journal of Structural Geology*, vol. 23, no. 2-3, pp. 507–520, 2001.

[18] N. Mortimer and B. P. Roser, "Geochemical evidence for the position of the Caples–Torlesse boundary in the Otago Schist, New Zealand," *Journal of the Geological Society, London*, vol. 149, no. 6, pp. 967–977, 1992.

[19] Å. Fagereng, "Fractal vein distributions within a fault-fracture mesh in an exhumed accretionary mélange, Chrystalls Beach Complex, New Zealand," *Journal of Structural Geology*, vol. 33, no. 5, pp. 918–927, 2011.

[20] Å. Fagereng and A. F. Cooper, "The metamorphic history of rocks buried, accreted and exhumed in an accretionary prism: an example from the Otago Schist, New Zealand," *Journal of Metamorphic Geology*, vol. 28, no. 9, pp. 935–954, 2010.

[21] I. J. Graham and N. Mortimer, "Terrane characterisation and timing of metamorphism in the Otago Schist, New Zealand, using Rb-Sr and K-Ar geochronology," *New Zealand Journal of Geology and Geophysics*, vol. 35, no. 4, pp. 391–401, 1992.

[22] C. J. Adams and I. J. Graham, "Age of metamorphism of Otago Schist in eastern Otago and determination of protoliths from initial strontium isotope characteristics," *New Zealand Journal of Geology and Geophysics*, vol. 40, no. 3, pp. 275–286, 1997.

[23] C. J. Adams and R. Maas, "Age/isotopic characterisation of the Waipapa Group in Northland and Auckland, New Zealand, and implications for the status of the Waipapa Terrane," *New Zealand Journal of Geology and Geophysics*, vol. 47, no. 2, pp. 173–187, 2010.

[24] C. J. Adams, H. J. Cambell, and W. L. Griffin, "Provenance comparisons of Permian to Jurassic tectonostratigraphic terranes in New Zealand: perspectives from detrital zircon age patterns," *Geological Magazine*, vol. 144, no. 4, pp. 701–729, 2007.

[25] E. J. Scanlan, J. M. Scott, V. J. Wilson, C. H. Stirling, M. R. Reid, and P. J. Le Roux, "In situ 87Sr/86Sr of scheelite and calcite reveals proximal and distal fluid-rock interaction during orogenic W-Au mineralization, Otago Schist, New Zealand," *Economic Geology*, vol. 113, no. 7, pp. 1571–1586, 2018.

[26] N. Mortimer, "Metamorphic zones, terranes, and Cenozoic faults in the Marlborough Schist, New Zealand," *New Zealand Journal of Geology and Geophysics*, vol. 36, no. 3, pp. 357–368, 1993.

[27] T. A. Little, N. Mortimer, and M. McWilliams, "An episodic Cretaceous cooling model for the Otago-Marlborough Schist, New Zealand, based on40Ar/39Ar white mica ages," *New Zealand Journal of Geology and Geophysics*, vol. 42, no. 3, pp. 305–325, 1999.

[28] D. R. Gray and D. A. Foster, "$^{40}Ar/^{39}Ar$ thermochronologic constraints on deformation, metamorphism and cooling/exhumation of a Mesozoic accretionary wedge, Otago Schist, New Zealand," *Tectonophysics*, vol. 385, no. 1–4, pp. 181–210, 2004.

[29] J. B. Jacob, J. M. Scott, I. M. Turnbull, M. S. Tarling, and M. W. Sagar, "High- to ultrahigh-temperature metamorphism in the lower crust: an example resulting from Hikurangi Plateau collision and slab rollback in New Zealand," *Journal of Metamorphic Geology*, vol. 35, no. 8, pp. 831–853, 2017.

[30] M. A. Forster and G. S. Lister, "Cretaceous metamorphic core complexes in the Otago Schist, New Zealand," *Australian Journal of Earth Sciences*, vol. 50, no. 2, pp. 181–198, 2003.

[31] R. Weinberger, Y. Eyal, and N. Mortimer, "Formation of systematic joints in metamorphic rocks due to release of residual elastic strain energy, Otago Schist, New Zealand," *Journal of Structural Geology*, vol. 32, no. 3, pp. 288–305, 2010.

[32] R. J. Norris, P. O. Koons, and A. F. Cooper, "The obliquely-convergent plate boundary in the South Island of New Zealand: implications for ancient collision zones," *Journal of Structural Geology*, vol. 12, no. 5-6, pp. 715–725, 1990.

[33] I. M. Turnbull, D. Craw, and R. J. Norris, "Pre-miocene and post-miocene deformation in the Bannockbum basin, Central Otago, New Zealand," *New Zealand Journal of Geology and Geophysics*, vol. 36, no. 1, pp. 107–115, 1993.

[34] N. J. Litchfield, "The Titri Fault System: Quaternary-active faults near the leading edge of the Otago reverse fault province," *New Zealand Journal of Geology and Geophysics*, vol. 44, no. 4, pp. 517–534, 2001.

[35] B. I. Taylor-Silva, M. W. Stirling, N. J. Litchfield, J. D. Griffen, E. J. van den Berg, and N. Wang, "Paleoseismology of the Akatore Fault, Otago, New Zealand," *New Zealand Journal of Geology and Geophysics*, vol. 63, no. 2, pp. 151–167, 2020.

[36] R. J. Norris and R. M. Carter, "Fault-bounded blocks and their role in localising sedimentation and deformation adjacent to the alpine fault, southern New Zealand," *Tectonophysics*, vol. 87, no. 1-4, pp. 11–23, 1982.

[37] M. Reyners, C. E. Ingham, and B. G. Ferris, "Microseismicity of the upper Clutha valley, South Island, New Zealand," *New Zealand Journal of Geology and Geophysics*, vol. 26, no. 1, pp. 1–6, 1983.

[38] C. H. Scholtz, L. R. Sykes, and Y. P. Aggarwal, "Earthquake prediction: a physical basis," *Science*, vol. 181, no. 4102, pp. 803–810, 1973.

[39] R. H. Sibson, F. Ghisetti, and J. Ristau, "Stress control of an evolving strike-slip fault system during the 2010-2011 Canterbury, New Zealand, earthquake sequence," *Seismological Research Letters*, vol. 82, no. 6, pp. 824–832, 2011.

[40] R. H. Sibson, F. C. Ghisetti, and R. A. Crookbain, "Andersonian wrench faulting in a regional stress field during the

2010 – 2011 Canterbury, New Zealand, earthquake sequence," *Geological Society, London, Special Publications*, vol. 376, no. 1, pp. 7–18, 2012.

[41] J. Townend, S. Sherburn, R. Arnold, C. Boese, and L. Woods, "Three-dimensional variations in present-day tectonic stress along the Australia–Pacific plate boundary in New Zealand," *Earth and Planetary Science Letters*, vol. 353-354, pp. 47–59, 2012.

[42] E. Warren-Smith, S. Lamb, T. A. Stern, and E. Smith, "Microseismicity in Southern South Island, New Zealand: implications for the mechanism of crustal deformation adjacent to a major continental transform," *Journal of Geophysical Research: Solid Earth*, vol. 122, no. 11, pp. 9208–9227, 2017.

[43] N. Mortimer, S. McLaren, and W. J. Dunlap, "Ar-Ar dating of K-feldspar in low grade metamorphic rocks: example of an exhumed Mesozoic accretionary wedge and forearc, South Island, New Zealand," *Tectonics*, vol. 31, no. 3, 2012.

[44] D. Delvaux and B. Sperner, "New aspects of tectonic stress inversion with reference to the TENSOR program," *Geological Society, London, Special Publications*, vol. 212, no. 1, pp. 75–100, 2003.

[45] C. Pin, A. Gannoun, and A. Dupont, "Rapid, simultaneous separation of Sr, Pb, and Nd by extraction chromatography prior to isotope ratios determination by TIMS and MC-ICP-MS," *Journal of Analytical Atomic Spectrometry*, vol. 29, no. 10, pp. 1858–1870, 2014.

[46] J. M. Scott, A. Pontesilli, M. Brenna et al., "The Dunedin Volcanic Group and a revised model for Zealandia's alkaline intraplate volcanism," *New Zealand Journal of Geology and Geophysics*, pp. 1–20, 2020.

[47] T. Tanaka, S. Togashi, H. Kamioka et al., "JNdi-1: a neodymium isotopic reference in consistency with LaJolla neodymium," *Chemical Geology*, vol. 168, no. 3-4, pp. 279–281, 2000.

[48] A. Coote, P. Shane, C. Stirling, and M. Reid, "The origin of plagioclase phenocrysts in basalts from continental monogenetic volcanoes of the Kaikohe-Bay of Islands field, New Zealand: implications for magmatic assembly and ascent," *Contributions to Mineralogy and Petrology*, vol. 173, no. 2, 2018.

[49] C. J. Adams and P. Robinson, "Potassium-argon age studies of metamorphism/uplift/cooling in Haast Schist coastal sections south of Dunedin, Otago, New Zealand," *New Zealand Journal of Geology and Geophysics*, vol. 36, no. 3, pp. 317–325, 1993.

[50] M. Burkhard, "Calcite twins, their geometry, appearance and significance as stress-strain markers and indicators of tectonic regime: a review," *Journal of Structural Geology*, vol. 15, no. 3-5, pp. 351–368, 1993.

[51] S.-S. Sun and W. F. McDonough, "Chemical and isotopic systematics of oceanic basalts: implications for mantle composition and processes," *Geological Society, London, Special Publications*, vol. 42, no. 1, pp. 313–345, 1989.

[52] R. H. Groshong Jr., "Calcite twin morphology: a low-temperature deformation geothermometer," *Geological Society of America Bulletin*, vol. 100, pp. 1329–1360, 1988.

[53] D. A. Ferrill, A. P. Morris, M. A. Evans, M. Burkhard, R. H. Groshong Jr., and C. M. Onasch, "Calcite twin morphology: a low-temperature deformation geothermometer," *Journal of Structural Geology*, vol. 26, no. 8, pp. 1521–1529, 2004.

[54] G. R. T. Jenkin, D. Craw, and A. E. Fallick, "Stable isotopic and fluid inclusion evidence for meteoric fluid penetration into an active mountain belt; Alpine Schist, New Zealand," *Journal of Metamorphic Geology*, vol. 12, no. 4, pp. 429–444, 1994.

[55] P. O. Koons, D. Craw, S. C. Cox, P. Upton, A. S. Templeton, and C. P. Chamberlain, "Fluid flow during active oblique convergence: a Southern Alps model from mechanical and geochemical observations," *Geology*, vol. 26, no. 2, pp. 159–162, 1998.

[56] F. Ghisetti and R. H. Sibson, "Accommodation of compressional inversion in north-western South Island (New Zealand): old faults versus new?," *Journal of Structural Geology*, vol. 28, no. 11, pp. 1994–2010, 2006.

[57] N. J. Litchfield and R. J. Norris, "Holocene motion on the Akatore Fault, south Otago coast, New Zealand," *New Zealand Journal of Geology and Geophysics*, vol. 43, no. 3, pp. 405–418, 2000.